Magnetotransport in Electron Waveguides

by

Thalia L. Rich

Submitted to the Department of Electrical Engineering and Computer Science
in partial fulfillment of the requirements for the degree of

Master of Science

at the

MASSACHUSETTS INSTITUTE OF TECHNOLOGY

February 1994

© Massachusetts Institute of Technology 1994. All rights reserved.

Author .....
Department of Electrical Engineering and Computer Science
January 28, 1994

Certified by ....
Jesús A. del Alamo
Associate Professor of Electrical Engineering
Thesis Supervisor

Accepted by .....
F. M. Morgenthaler
Professor of Electrical Engineering
Chairman, Departmental Committee on Graduate Students

MASSACHUSETTS INSTITUTE OF TECHNOLOGY
MIT LIBRARIES
APR 06 1994
LIBRARIES

Magnetotransport in Electron Waveguides

by

Thalia L. Rich

Submitted to the Department of Electrical Engineering and Computer Science
on January 28, 1994, in partial fulfillment of the
requirements for the degree of
Master of Science

Abstract

Fundamental understanding of quantum-mechanical transport is necessary as devices are scaled down to the order of the electron Fermi wavelength, λ_F. Electron waveguide devices, with both two-dimensional (2D) and one-dimensional (1D) transport regimes, represent a particularly ideal system to explore the physics of transport in the quantum regime. Additional electron transport physics can be learned by studying the impact of a magnetic field on the conductance of an electron waveguide. This work explores magnetotransport of electron waveguides by examining the low-temperature magnetoconductance behavior of a split-gate electron waveguide fabricated on an AlGaAs/GaAs modulation-doped heterostructure. In the 2D regime, we experimentally verify the existence of three theoretically-predicted magnetic field regimes (low-field classical Hall regime, high-field classical Hall regime, and quantum Hall regime). In addition, the experimental conductance behavior in each of these regimes quantitatively agrees very well with theory. In the 1D regime, we also observe clear experimental evidence of three magnetic field regimes predicted by theory (low-field regime, magnetic depopulation regime, and quantum Hall regime) with a conductance behavior that agrees qualitatively with prediction. A quantitative analysis of these regimes, however, requires detailed understanding of the shape of the electrostatic potential that defines the waveguide and its evolution with gate voltage. Self-consistent Poisson/Schrodinger simulations show that this potential is complex and cannot be easily approximated by a simple analytical function. This makes quantitative analysis difficult.

Thesis Supervisor: Jesús A. del Alamo
Title: Associate Professor of Electrical Engineering

Acknowledgements

I first must thank my advisor, Professor Jesús del Alamo, whose energy, enthusiasm, and dedication to excellence are inspiring. I have learned a great deal in the course of my thesis and look forward to continuing my work with him in the future.

I also owe thanks to Dr. Cristopher Eugster for passing on to me his hard-earned knowledge and experience. Cris spent a great deal of time training me when he was busy with his own work and for this I am grateful.

The devices I measured were fabricated by Cris Eugster on material provided by Professor Michael Melloch of Purdue University. Electron beam lithography was carried out by Dr. Michael Rooks of the National Nanofabrication Facility at Cornell University.

The self-consistent Poisson/Schrodinger solver was written by Dr. Greg Snider, who also provided invaluable assistance with the simulations.

I have had useful technical discussions with Professors Qing Hu, Marc Kastner, Terry Orlando, and Xiao-Gang Wen. I appreciate the time they took to speak with me.

Thanks are also due to David Greenberg and Mark Somerville, for countless discussions about waveguides, physics, and everything else under the sun. David deserves an extra round of applause for tirelessly resolving computer dilemmas. Best wishes for abundant data to the entire research group: David, Peter Nuytkens, Mark, Akbar Moolji, Matt Sinn, Jim Reiner, and Tracy Adams.

Angela Odoardi and Charmaine Cudjoe help keep my day-to-day existence at MIT enjoyable and relatively paper-work free.

My studies at MIT have been funded by a departmental fellowship and a National Defense Science and Engineering graduate fellowship. The research has been partly sponsored by the National Science Foundation through Presidential Young Investigator Award number 9157305-ECS and a contract with Nippon Telegraph and Telephone Corporation.

On a personal note, thanks to the McCants family and my friends at Green Hall for making me feel at home in Cambridge. Special thanks to Helen Hwang (H^4) for friendship and, above all, a sense of humor. Thanks to all of my friends for love and support.

Finally, my eternal gratitude to my parents, for everything.

Contents

1 Introduction **8**

2 Theory of Magnetotransport in Electron Waveguides **14**

2.1 Introduction 14

2.2 2D Regime 15

2.2.1 Zero-field 16

2.2.2 Low-field and High-field Classical Hall Regimes 17

2.2.3 Quantum Hall Regime 21

2.3 1D Regime 24

2.3.1 Zero-field Regime 25

2.3.2 Low-field Regime 27

2.3.3 Magnetic Depopulation Regime 29

2.3.4 Quantum Hall Regime 30

2.4 Transition from 2D to 1D 30

2.5 Summary 31

3 Experimental Data **32**

3.1 Introduction 32

3.2 Device Description and Experimental Technique 32

3.3 Experimental Results and Discussion 34

3.3.1 Conductance Versus Top-Gate Voltage for Discrete Magnetic Field Values 35

3.3.2 Conductance Versus Magnetic Field for Discrete Top Gate Voltages . . . 39
3.4 Summary . . . 40

4 Comparison of Simulated, Experimental, and Theoretical Data 42
4.1 Introduction . . . 42
4.2 Zero-field Simulation of Electron Waveguides . . . 42
4.2.1 Fitting Parameters . . . 43
4.2.2 Thermal and Voltage Window Smearing . . . 44
4.2.3 Simulated Conductance . . . 44
4.2.4 Examination of the Potential Shape . . . 46
4.3 Discussion and Comparison of Simulated, Experimental, and Theoretical Data . . . 47
4.3.1 2D Regime . . . 48
4.3.2 1D Regime . . . 53
4.4 Summary . . . 58

5 Conclusion 59

List of Figures

1-1 Split-gate and electron gas configuration in an electron waveguide[3] . . 9

1-2 Current/voltage characteristic for a typical waveguide showing the 2D and 1D regimes. The inset details the 1D regime.[3] 10

2-1 Transformation of density of states from 2D to 0D Landau levels. . . 18

2-2 $R_{2t}\sigma_0$, $\frac{L}{W}\rho_{xx}\sigma_0$, and $\rho_{xy}\sigma_0$ versus scaled magnetic field for a mesa with $\frac{L}{W} = 10$. 20

2-3 G_{2t}/σ_0, $\frac{W}{L}\sigma_{xx}/\sigma_0$, and σ_{yx}/σ_0 versus magnetic field for a mesa with $\frac{W}{L} = 10$. 20

2-4 Energy of Landau levels vs. k_x for an infinite 2DEG. 22

2-5 Energy of Landau levels vs. k_x for a 2DEG with edges. 23

2-6 Illustration of interior and skipping orbits for a 2DEG with edges in the quantum Hall regime. 24

2-7 Illustration of energy levels for 1D subbands in an electron waveguide.[3] 25

2-8 Quantized conductance for an electron waveguide in the 1D region.[3] . 27

3-1 Cross-section of AlGaAs/GaAs heterostructure[3] 33

3-2 Mesa layout of electron waveguide. 34

3-3 Measurement setup schematic.[3] Wavy line represents waveguide. . . . 35

3-4 Conductance versus top-gate voltage with zero magnetic field for three experimental runs. The inset shows the quantized conductance steps in the 1D region. 36

3-5 Conductance versus top-gate voltage for the first experimental run. . 37

3-6 Conductance versus top-gate voltage for the second experimental run. 37

3-7 Conductance versus top-gate voltage for the third experimental run. . 38
3-8 Conductance versus magnetic field for various top-gate voltages. . . . 39
3-9 Conductance versus inverse magnetic field for various top-gate voltages. 40

4-1 Simulated and experimental conductances versus top-gate voltage . . 45
4-2 The electrostatic potential across the waveguide. The shaded regions show the position of the split-gate and the inset zooms in on the gap between the gates. 47
4-3 Energy difference between the second and third subband divided by the energy difference between the first and second subband for the simulated structure and parabolic and square wells versus top-gate voltage. 48
4-4 Measured and predicted conductance versus magnetic field for zero top-gate voltage. 50
4-5 Derivative of conductance versus magnetic field for $V_{tg} = 0V$. Inset details onset of oscillations. 51
4-6 Plateau index versus inverse magnetic field at the onset of each plateau for zero top-gate voltage. 52
4-7 n_s for various top-gate voltages in the 2D regime as computed from experimental data and by simulation. 53
4-8 Derivative of conductance with respect to top-gate voltage for the second experimental run. 54
4-9 Step height versus magnetic field for the second experimental run. . . 55
4-10 Top-gate voltage versus magnetic field for the onset of subbands for the second experimental run. 56
4-11 Top-gate voltage versus magnetic field for the onset of subbands for the third experimental run. 57
4-12 Plateau index versus inverse magnetic field for top-gate voltages in the 1D regime. 58

Chapter 1

Introduction

As devices are scaled down to increase speed and packing density, lateral device dimensions become smaller than the electron mean free path and approach the order of the Fermi wavelength of the electron. On this scale, electrons are confined in the lateral direction and their wave nature becomes prominent. Such devices can no longer be described by classical transport models and ballistic quantum-mechanical transport models must be used to characterize these devices.

Electron waveguide devices, which allow electron motion in only one direction, have been used to study the physics of quantum-mechanical transport. To observe quantum effects, the width of a waveguide must be on the order of the electron Fermi wavelength and the length must be less than the electron mean free path so that electron motion is coherent along the waveguide.[1] Typically, electron waveguide devices have been implemented using split-gate field-effect transistors fabricated on modulation-doped III-V heterostructures, which have demonstrated very high mobilities and hence large mean free paths.[2] The heterostructure confines electrons to a quasi-two-dimensional electron gas (2DEG) and the split-gates provide lateral confinement under proper bias conditions. A split-gate electron waveguide schematic is shown in Fig 1-1.[3]

At zero gate voltage, the 2DEG formed at the insulator/channel boundary of the heterostructure is of uniform density everywhere. As the gate voltage is lowered, the electron gas below the split-gates is depleted and a quasi-1D waveguide is formed

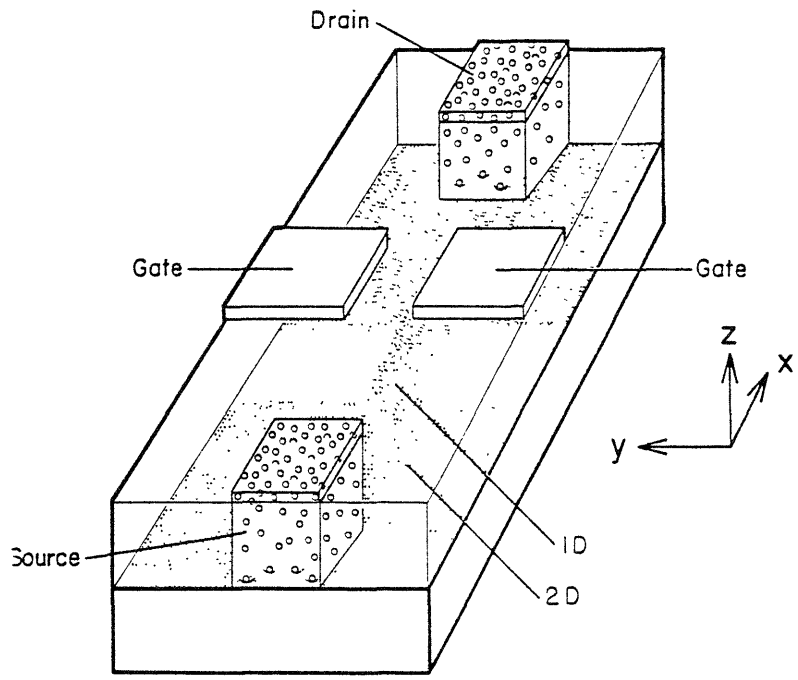

Figure 1-1: Split-gate and electron gas configuration in an electron waveguide[3].

underneath the gap between the gates. The two-dimensional threshold voltage, V_{th}^{2D}, is the voltage at which the electron gas is entirely depleted directly beneath the gates and the quasi-1D waveguide is first formed. As the gate voltage is lowered further, fringing fields deplete the electrons in the waveguide until it is pinched off. The one-dimensional threshold voltage, V_{th}^{1D}, is the voltage at which the electrons beneath the gap between the gates have been completely depleted. Fig. 1-2 shows the current/voltage relation for a typical waveguide. Clearly, for this device, $V_{th}^{2D} \simeq$ -0.5 V and $V_{th}^{1D} \simeq$ -1.7 V. The slope of the current changes below V_{th}^{2D} because the sideways depletion of electrons in the waveguide in the 1D regime is much slower than the downward depletion of electrons below the gates in the 2D regime. Because transport in split-gate waveguides is of a 2D type for voltages above $V_{th}^{2D}$and a 1D type for voltages between V_{th}^{2D} and V_{th}^{1D}, these devices can be used to study the physics of both 2D and 1D transport.

Analogous to an optical waveguide that confines electromagnetic waves in two dimensions, an electron waveguide confines electrons in two dimensions. Just as transverse modes arise in an optical waveguide as described by Maxwell's equations,

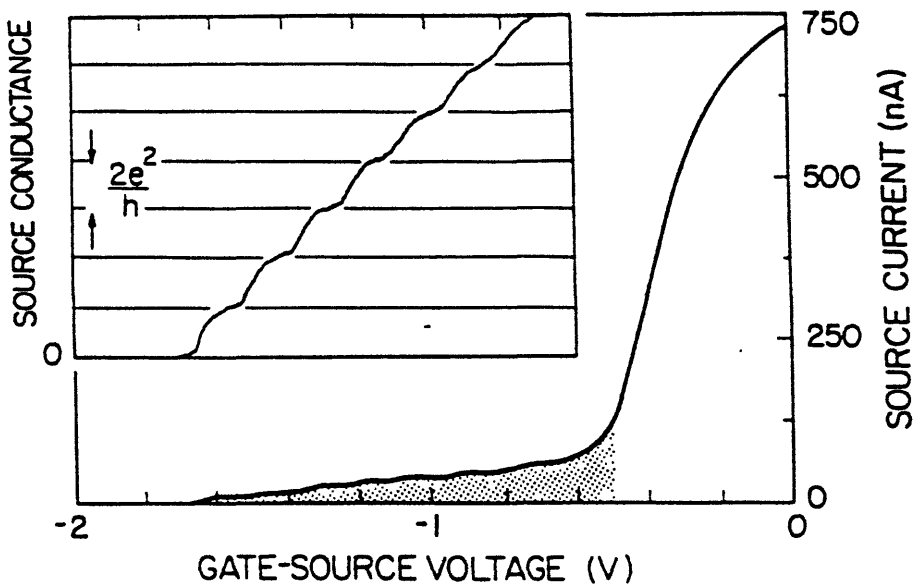

Figure 1-2: Current/voltage characteristic for a typical waveguide showing the 2D and 1D regimes. The inset details the 1D regime.[3].

modes arise in an electron waveguide as described by Schrodinger's equation. Under the proper condition, each of these modes, or subbands, contributes a conductance of $2e^2/h$. Therefore, the total conductance of an electron waveguide is equal to $2e^2/h$ multiplied by the number of occupied modes. Furthermore, the conductance quanta, $\frac{2e^2}{h}$, is a physical constant, independent of device geometry and material parameters.

In the split-gate geometry, the gate voltage modulates the width of the waveguide, which determines the number of occupied modes. When the gate voltage is decreased, the waveguide gets narrower, successive modes get pinched off, and the conductance decreases by $2e^2/h$ as each mode is shut off. This is shown in the inset of Fig. 1-2, which graphs the conductance as a function of gate-source voltage for an electron waveguide.[3] Quantized conductance of an electron waveguide was first discovered in 1988.[4,5]

The application of magnetic field to a waveguide provides a way to learn more about electron transport. Magnetic field measurements can provide information about some characteristics of the waveguide such as the shape of the electrostatic potential

that defines the waveguide, as well as reveal new magnetic-field-induced phenomena. When a magnetic field is applied perpendicular to the 2DEG along the direction of the heterostructure growth, electrons tend to circle in cyclotron orbits with cyclotron radii inversely proportional to the field. The effect on conductance is dependent upon the relative size of the cyclotron orbits compared with the dimension of the potential well confining the electrons. Thus, the transport physics and hence the magnetoconductance behavior is fundamentally different in the 2D and 1D regimes of the waveguide.

In the 2D regime, where device dimensions are typically greater than the mean free path of electrons, transport is diffusive and zero-field conductivity depends upon electron concentration and mobility. As mentioned above, when a magnetic field is applied, the electrons tend to circle in orbits with radii inversely proportional to the field. If the cyclotron radius is much larger than the mean free path, electrons will scatter after only completing a small fraction of a full orbit, so transport remains diffusive and the conductivity in the field direction is not affected. This is known as the low-field classical Hall regime. When the field is increased so that the cyclotron radius is much smaller than the mean free path, an electron can complete many orbits without scattering so the electrons become trapped in cyclotron orbits and conductivity in the direction of the field drops. This is the high-field classical Hall regime.

Due to magnetic confinement, the 2D density of states is transformed to a series of delta functions called Landau levels, whose energy separation is proportional to the magnetic field. When the field is strong enough that the separation between Landau levels is greater than the thermal smearing, the magnetic field dependence of the density of states can be seen in the behavior of the conductance.[6] In the high-field limit, the electrons away from the edges of the device are tightly bound in cyclotron orbits and do not contribute to conduction at all. Only electrons that scatter off the edges contribute to conduction. These edge channels, or edge states give rise to the quantum Hall effect,[7] in which each occupied edge channel contributes $\frac{2e^2}{h}$ to the conductance.[8] For this reason, this regime is known as the quantum Hall regime.

In the 1D regime, at zero magnetic field, device transversal dimensions are on the order of the Fermi wavelength and quasi-1D modes form in the device. Each mode contributes $\frac{2e^2}{h}$ to the conductance. As in the 2D case, when a magnetic field is applied, the electrons tend to circle in orbits. In the low field regime, the cyclotron radius is much larger than the waveguide, so the quantized conductance is not affected. As the field is increased so that the cyclotron radius is on the order of the waveguide, the magnetic field confinement becomes significant. The increased confinement leads to wider spaced energy levels and the magnetic field begins to depopulate subbands in the waveguide. This is known as the magnetic depopulation regime. At even higher fields, the cyclotron radius becomes much smaller than the waveguide, so the magnetic confinement is dominant and device dimensions become unimportant. This is the quantum Hall regime, and the conductance behavior will be the same as for a 2D sample in the quantum Hall regime.

Much work has been done on the magnetoconductance behavior of electron waveguides. Depopulation of the resulting magnetoelectric subbands and a transition to the quantum Hall effect regime at high field have been observed.[9,10] Models of the electrostatic potential that may be used to predict the depopulation of the subbands have been proposed and compared with experimental results.[9–12] Models that explain the transition to the quantum Hall effect regime have also been presented.[13]

Many of the studies of electron waveguides under a magnetic field have focused on multiple-probe measurements which, while ideal for investigating the physics of transport, are fundamentally different from two-terminal measurements. Because electron waveguide devices have (with the exception of the gates) only two terminals, a study of the two-terminal characteristics of these devices under a magnetic field is very relevant. This is the purpose of this thesis. We present a study of the two-terminal magnetoconductance characteristics of an split-gate electron waveguide fabricated[3] on a AlGaAs/GaAs modulation-doped heterostructure.[2]

In Chapter 2, we examine the theory of magnetotransport in electron waveguides, considering both the 2D and 1D regimes. In the 2D regime, we examine the conductance behavior in the low-field and high-field classical Hall regimes and the quantum

Hall regime. We consider in detail geometry issues in the classical Hall regimes and the implications of Landau levels in the quantum Hall regime as well as the boundaries between the magnetic field regimes. In the 1D regime, we explore the origin of quantized conductance in zero magnetic field. Using an approximation to the electrostatic potential that defines the waveguide, we examine the three magnetic field regimes and generalize our conclusions to a more realistic electrostatic potential.

Experimental techniques and results of two sets of experiments are presented in Chapter 3. In the first set of experiments, two-terminal conductance as a function of gate voltage is measured at various values of magnetic field. In the second set, two-terminal conductance as a function of magnetic field is measured at various gate voltages. These experiments enable us to clearly see the different gate voltage and magnetic field regimes.

In Chapter 4, we simulate a typical split-gate electron waveguide using a computer program developed by G.L. Snider[14] that self-consistently solves Poisson's equation and Schrodinger's equation. Using the simulation results, we calculate conductance as a function of gate voltage and explore the shape of the electrostatic potential that defines the waveguide. Finally, we compare the theoretical and experimental predictions in the various gate voltage and magnetic field regimes. We find that experimental and theoretical conductance behavior agree very well in the 2D regime. In the 1D regime, we see clear experimental evidence of the three theoretically predicted magnetic field regimes. Quantitative analysis of these regimes proves to be difficult because it requires detailed knowledge of the complex electrostatic potential that defines the waveguide and its functional relation to gate voltage, which is not easily determined.

Chapter 5 summarizes the main conclusions of this thesis.

Chapter 2

Theory of Magnetotransport in Electron Waveguides

2.1 Introduction

In this chapter we examine the magnetotransport of split-gate electron waveguides when a magnetic field is applied perpendicular to the 2DEG. We consider the 2D and 1D regimes of the waveguide in detail and discuss the predicted conductance characteristics.

Transport in a 2DEG with dimensions much greater than the mean free path of electrons is diffusive, and its conductivity depends upon electron concentration and mobility. When a magnetic field is applied, electrons tend to circle in cyclotron orbits with radii inversely proportional to the field. If the field is small enough so that an electron scatters before it completes an orbit (*i.e.* the cyclotron radius is much larger than the mean free path), the transport is still diffusive and the conductivity is not affected. When the field is increased so that an electron can complete many orbits without scattering (*i.e.* the cyclotron radius is much smaller than the mean free path), the electrons become trapped in the cyclotron orbits and the conductivity in the direction of the electric field drops. Due to magnetic confinement, the 2D density of states is transformed to a series of delta functions (Landau levels), whose energy separation and density of states are proportional to the magnetic field. When

the field is strong enough that the separation between Landau levels is greater than the thermal energy smearing, the magnetic field dependence of the density of states can be seen in such conductance behavior as Shubnikov-de Haas oscillations.[6] In the high-field limit, the electrons away from the edges are tightly bound in cyclotron orbits and do not contribute to conduction at all. The only electrons that contribute to conduction are the ones that scatter off the edges. These edge channels, or edge states, give rise to the quantum Hall effect.

When device dimensions are smaller that the mean free path, transport is not diffusive, but ballistic. In addition, if device transversal dimensions are reduced to the order of the Fermi wavelength, quasi-1D modes form and conductance becomes quantized in the number of occupied modes or subbands. We do not expect small fields (fields such that the cyclotron radius is much bigger than the device transversal dimensions) to affect the quantized conductance. As the field is increased so that the cyclotron radius is on the order of device dimensions, we expect the number of occupied modes and therefore the conductance to be affected by magnetic field. At even higher fields, when the cyclotron radius becomes much smaller than the device dimensions, the magnetic confinement is very strong and the device dimensions become unimportant, so we expect to see the same high-field behavior as in a large 2D sample.

The following sections study the theory of magnetic-field behavior of electron waveguides in both the 2D regime, where transport is diffusive, and the 1D regime, where transport is ballistic.

2.2 2D Regime

In this section we consider only the case of zero applied gate voltage, where the sheet carrier concentration is uniform over the entire sample. The transition from the 2D to the 1D regime is much more complicated and is briefly considered in Section 2.4. As discussed above, in the 2D regime there are three magnetic field regimes. They are known as the low-field classical Hall regime (cyclotron radius larger than the

mean free path), the high-field classical Hall regime (cyclotron radius smaller than the mean free path but Landau level separation less than thermal smearing), and the quantum Hall regime (Landau level separation greater than the thermal smearing). We examine the conductance behavior in the 2D regimes as the magnetic field is increased from zero through the three magnetic field regimes.

2.2.1 Zero-field

When the split-gate is at zero voltage, the electron gas is uniform over the whole mesa and transport is diffusive because the mesa is larger than the mean free path. In this case, the two-terminal conductivity, σ, from source to drain is given by the Drude conductivity formula:[15]

$$\sigma(B=0) = \sigma_0 = \frac{n_s e^2 \tau}{m^*}, \tag{2.1}$$

where n_s is the two-dimensional electron concentration for zero gate voltage and τ is the electron scattering time.

It is not conductivity that one actually measures, but conductance. For a rectangular sample with width W and length L in the diffusive regime, the conductance, G, is given by:

$$G = \sigma_0 \frac{W}{L}. \tag{2.2}$$

In a more complicated geometry where there is no clear W or L, the factor (W/L) must be replaced by a suitable geometry factor. Therefore, the two-terminal conductance of a sample with arbitrary geometry at zero gate voltage is given by:

$$G = g\frac{n_s e^2 \tau}{m^*} \tag{2.3}$$

where g is a geometry-dependent factor.

2.2.2 Low-field and High-field Classical Hall Regimes

When a magnetic field ($\mathbf{B} = \nabla \times \mathbf{A}$) is applied perpendicular to a uniform 2DEG, the Hamiltonian becomes:

$$\mathcal{H} = \frac{(\mathbf{p} + e\mathbf{A})^2}{2m^*}. \tag{2.4}$$

It can be shown that in the Landau gauge ($\mathbf{A} = -By\hat{x}$), this reduces to a simple harmonic oscillator Hamiltonian in the y-direction (perpendicular to the waveguide) that has been translated in y by p_x/eB. The characteristic frequency, $\omega_c = eB/m^*$, is the cyclotron frequency, and the energy eigenvalues, $E_n = \left(n + \frac{1}{2}\right)\hbar\omega_c$ for $n = 0, 1, 2, ...$, are the Landau energy levels. In the absence of scattering, the density of states therefore collapses from a 2D density of states to a 0D density of states, which is simply a sum of delta functions:

$$g_{0D} = \frac{2eB}{h}\sum_{0}^{\infty}\delta\left(E - E_n\right). \tag{2.5}$$

A conceptual diagram of the transformation of the density of states including relevant energy scales is show in Fig. 2-1. Since the density of states of the 0D levels increases with magentic field, the position of the Landau levels with respect to the Fermi level changes with applied field. As the magnetic field is increased, the Landau levels spread out and they move up through the Fermi level so that electron concentration remains constant as the field is increased. If the Landau level separation ($\hbar\omega_c$) is much less than the thermal smearing (3.5 kT) and there are many occupied levels, the magnetic-field dependence of the density of states is not observable, and the density of states appears to be 2D. This regime is known as the *classical Hall regime.*

In the classical Hall regime, the density of states can be approximated as 2D and transport is still diffusive. Therefore, we can use the Drude model to describe the conductance. Furthermore, if the field is small enough that an electron scatters many times before it completes an orbit ($\omega_c\tau \ll 1$), then the magnetic field is negligible and the conductance in the low-field classical Hall regime is given by the zero-field conductance equation, Eq. 2.2. The condition $\omega_c\tau \ll 1$ is equivalent to the condition

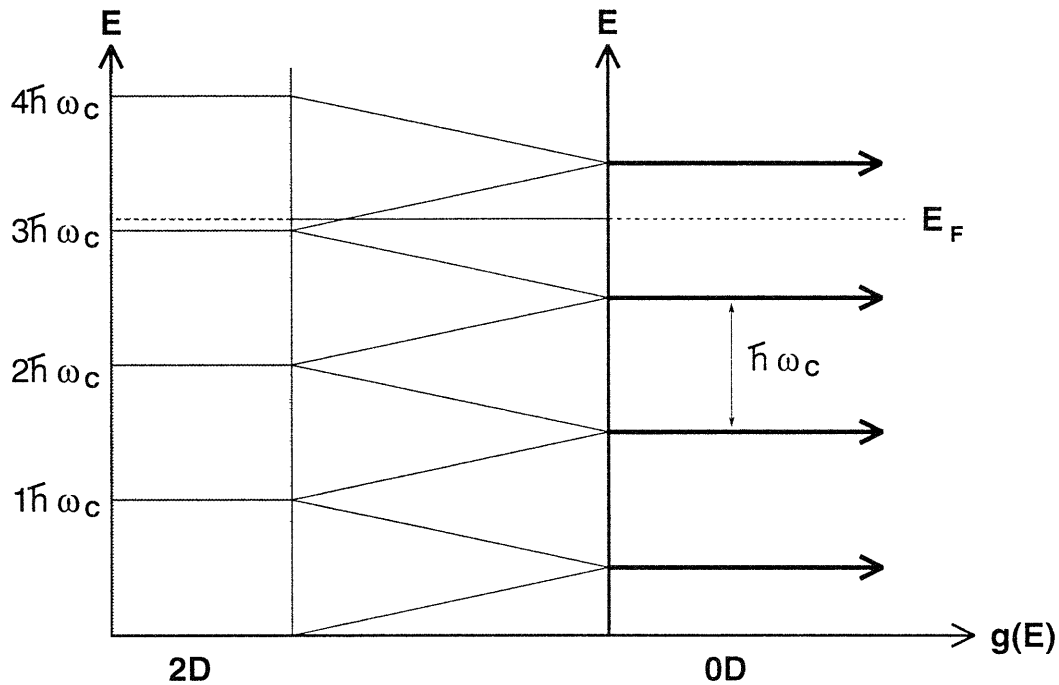

Figure 2-1: Transformation of density of states from 2D to 0D Landau levels.

$l_{cyc} \gg l$ where $l_{cyc} = \hbar k_F/eB$ is the cyclotron radius and $l = \hbar k_F \tau/m^*$ is the mean free path. Therefore, the *low-field classical Hall regime* is the regime where the mean free path is much smaller than the cyclotron radius.

In the *high-field classical Hall regime*, the magnetic field is high enough that the cyclotron radius is much smaller than the mean free path and magnetic phenomena can no longer be ignored. A component of the current perpendicular to the electric field arises due to the Lorentz force. The Drude conductivity formula thus becomes a conductivity tensor:[15]

$$\sigma = \frac{\sigma_0}{1 + (\omega_c \tau)^2} \begin{pmatrix} 1 & -\omega_c \tau \\ \omega_c \tau & 1 \end{pmatrix}, \tag{2.6}$$

or, given in terms of the resistivity tensor, ρ ($\rho = \sigma^{-1}$):

$$\rho = \frac{1}{\sigma_0} \begin{pmatrix} 1 & \omega_c \tau \\ -\omega_c \tau & 1 \end{pmatrix}. \tag{2.7}$$

where σ_0 is defined in Eq. 2.1.

As in the zero-field regime, the two-terminal conductance that one measures is not simply the conductivity. There is a geometry-dependent mixing of the transverse and longitudinal components of conductivity. For a long and narrow rectangular mesa ($L \gg W$), the empirical effect of this mixing (in terms of the components of the resistivity tensor) has been given as:[16]

$$R_{2t} = G_{2t}^{-1} = \frac{L}{W}\rho_{xx} + \rho_{xy}, \tag{2.8}$$

where

$$\rho_{xx} = \frac{1}{\sigma_0} \tag{2.9}$$

and

$$\rho_{xy} = \frac{\omega_c \tau}{\sigma_0}. \tag{2.10}$$

Analogously, for a short and wide mesa ($L \ll W$):[17]

$$G_{2t} = \frac{W}{L}\sigma_{xx} + \sigma_{yx}, \tag{2.11}$$

where

$$\sigma_{xx} = \frac{\sigma_0}{1 + (\omega_c \tau)^2} \tag{2.12}$$

and

$$\sigma_{yx} = \frac{\sigma_0 \omega_c \tau}{1 + (\omega_c \tau)^2}. \tag{2.13}$$

To understand the behavior of R_{2t} and G_{2t} with magnetic field, we plot normalized values of R_{2t}, $\frac{L}{W}\rho_{xx}$, and ρ_{xy} with $L/W = 10$ in Fig. 2-2 and G_{2t}, $\frac{W}{L}\sigma_{xx}$, and σ_{yx} with $W/L = 10$ in Fig. 2-3. We see from these figures that R_{2t} reduces to $\frac{L}{W}\rho_{xx}$ in the low-field limit and ρ_{xy} in the high-field limit. Similarly, G_{2t} reduces to $\frac{W}{L}\sigma_{xx}$ in low fields and σ_{yx} in high fields. We can also see from Eqs. 2.9 and 2.12 than at low fields such that $\omega_c \tau \ll 1$, $\sigma_{xx} \rightarrow {\rho_{xx}}^{-1} = \sigma_0$. This confirms that the conductance in the low-field classical Hall regime is given by the zero-field conductance.

For an arbitrary geometry, the geometry-dependent mixing in the above equations is more complicated, but we do expect the conductance to reduce to Eq. 2.3 in the

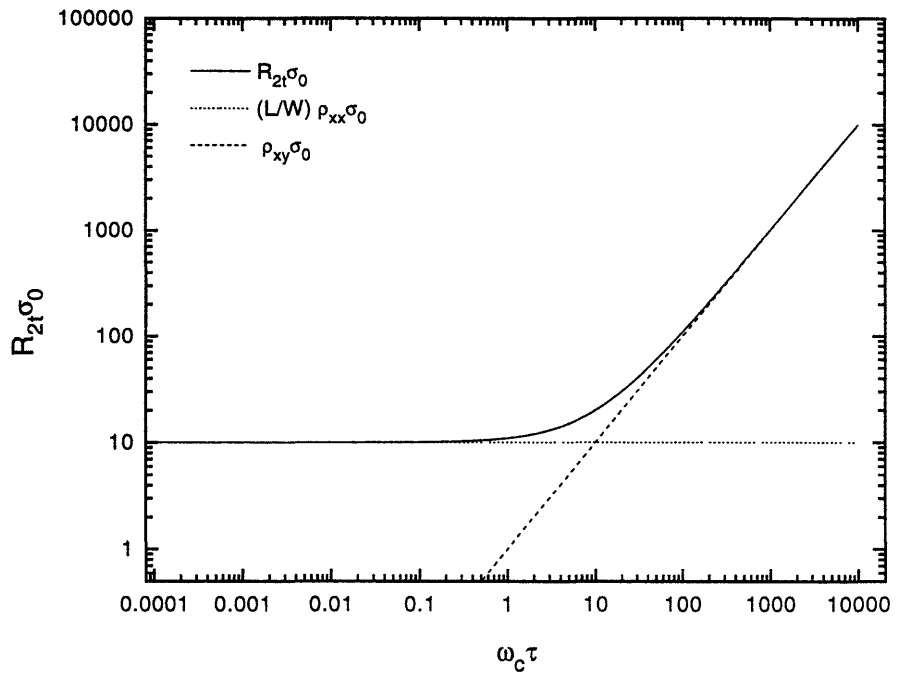

Figure 2-2: $R_{2t}\sigma_0$, $\frac{L}{W}\rho_{xx}\sigma_0$, and $\rho_{xy}\sigma_0$ versus scaled magnetic field for a mesa with $\frac{L}{W} = 10$.

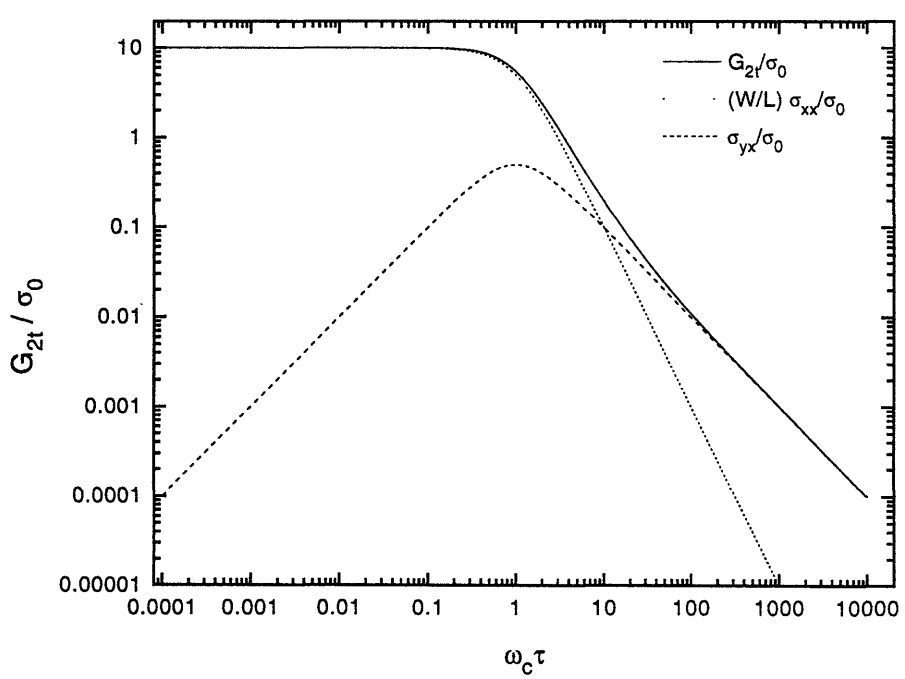

Figure 2-3: G_{2t}/σ_0, $\frac{W}{L}\sigma_{xx}/\sigma_0$, and σ_{yx}/σ_0 versus magnetic field for a mesa with $\frac{W}{L} = 10$.

low-field limit.

As discussed above, in the low-field classical Hall regime, $l_{cyc} \gg l$ ($\omega_c\tau \ll 1$), and the conductance reduces to the zero-field conductance. Physically, the electrons scatter before they complete a full orbit, so the conductance is not affected by the magnetic field. In the High-field classical Hall regime, l_{cyc} becomes on the order of l ($\omega_c\tau \simeq 1$), but the separation of the Landau levels is still smaller than the thermal smearing. In this regime, the conductance has a magnetic-field dependence that depends on the geometry. In general, though, we expect the conductance to fall off as electrons begin to get trapped in cyclotron orbits. We can see from Figs. 2-2 and 2-3 that the conductance does begin to fall off (resistance rises) near $\omega_c\tau = 1$

The work above is not valid when the magnetic field is so high that the 2D density of states is no longer a good approximation for the density of states. We discuss this regime in the next subsection.

2.2.3 Quantum Hall Regime

As discussed in the previous subsection, the Landau levels are separated by $\hbar\omega_c$ in energy. In the presence of a strong magnetic field ($B \gg B_{th}$ that corresponds to $\hbar\omega_c \simeq 3.5kT$), this energy spacing is greater than the thermal smearing, 3.5 kT,[18] and individual Landau levels can be resolved at the Fermi level. In this regime, known as the quantum Hall regime, the density of states can no longer be approximated as 2D; the 0D delta functions must be used. Shubnikov-de Haas oscillations in ρ_{xx}[6] and the quantum Hall effect in ρ_{xy},[7] both of which demonstrate the presence of Landau levels, have been observed at high fields.

Because of the geometry question discussed in the previous section, it is not obvious what a two-terminal measurement is actually measuring. In very high fields such that $l_{cyc} \ll l$ ($\omega_c\tau \gg 1$), Eqs. 2.8 and 2.11 reduce to:

$$G_{2t}\,(\omega_c\tau \gg 1) = \sigma_{yx}. \tag{2.14}$$

We therefore expect to see the quantum Hall effect, a transverse effect, in a two-

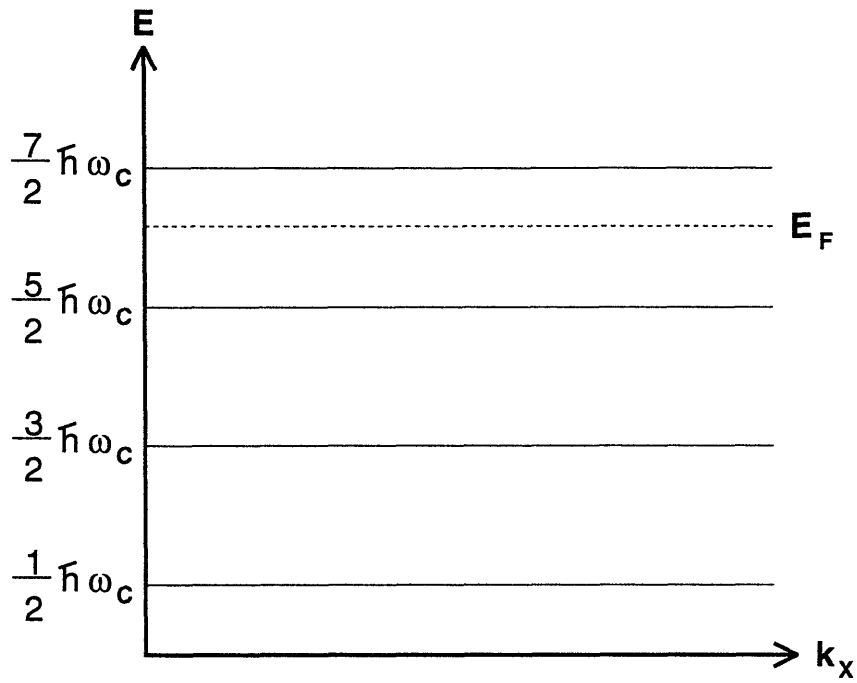

Figure 2-4: Energy of Landau levels vs. k_x for an infinite 2DEG.

terminal measurement at high fields. This has been observed and it has been proven that a two-terminal conductance measurement at high fields always yields the quantum Hall effect,[19,20] in which there are conductance plateaus at integral multiples of $\frac{2e^2}{h}$ as the magnetic field is varied. Thus, this high-field regime is known as the quantum Hall regime.

To explain why the two-terminal conductance is quantized at integral values of $\frac{2e^2}{h}$ in the quantum Hall regime, we must consider the formation of edge states. Fig. 2-4 shows the energy of Landau levels versus k_x for an infinite 2DEG. For a finite 2DEG, the infinite potential at the edges forces the electron wavefunction to zero at the edges. This means that the energy levels rise near the edges as shown in Fig. 2-5.[21]

For electrons away from the edges, the energies are the Landau level energies ($E_n = \left(n + \frac{1}{2}\right)\hbar\omega_c$), and the group velocity, $v(k_x) = \frac{1}{\hbar}\frac{dE}{dk_x}$ is zero. Therefore, these electrons are trapped in interior orbits and they do not carry current. The electrons near the edges are in states that do have a group velocity, so they do contribute to the current. It has been shown that each occupied edge state contributes $\frac{2e^2}{h}$ to the conductance.[8] Physically, these electrons are scattering forward off the walls in

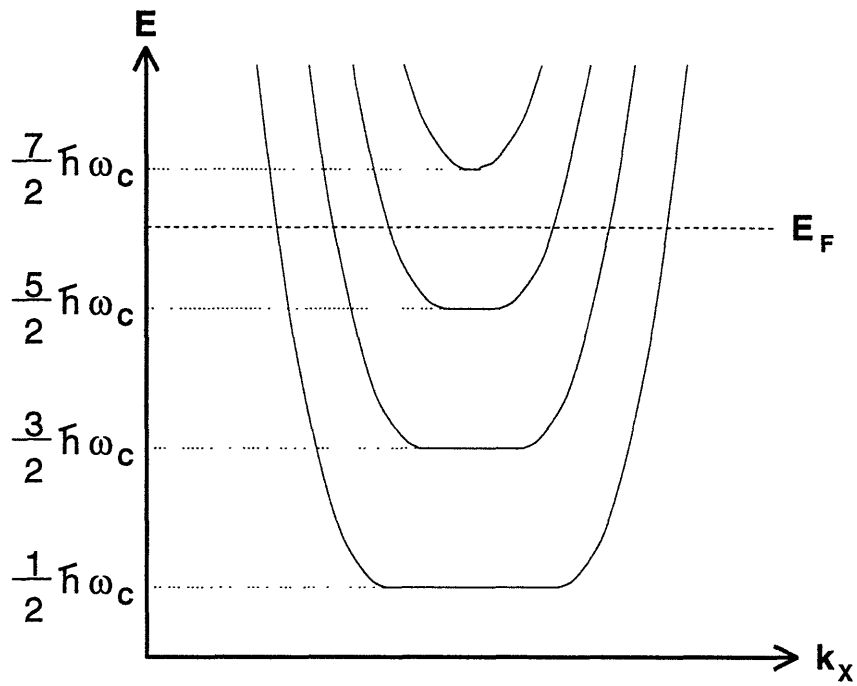

Figure 2-5: Energy of Landau levels vs. k_x for a 2DEG with edges.

skipping orbits.[13] An illustration of electron interior and skipping orbits is shown in Fig. 2-6.

Thus, in the quantum Hall regime, the conductance is given by:

$$G = \sum_{i=1}^{n} \frac{2e^2}{h} = n\frac{2e^2}{h}, \tag{2.15}$$

where n is the number of occupied Landau levels, given by:

$$n = Integer\left(\frac{E_F}{\hbar\omega_c} - \frac{1}{2}\right). \tag{2.16}$$

The number of occupied modes, and hence the conductance is modulated by the magnetic field. The rate at which the edge channels are depopulated by the magnetic field depends on the rate at which the Landau levels are swept through the Fermi level. From Eq. 2.5, we see that the Fermi level lines up with the Landau level n when $B_n = n_s h/2en$. Therefore the number of Landau levels that are occupied is periodic in $1/B$ with a period given by:

$$T_{1/B} = \frac{2e}{n_s h}. \tag{2.17}$$

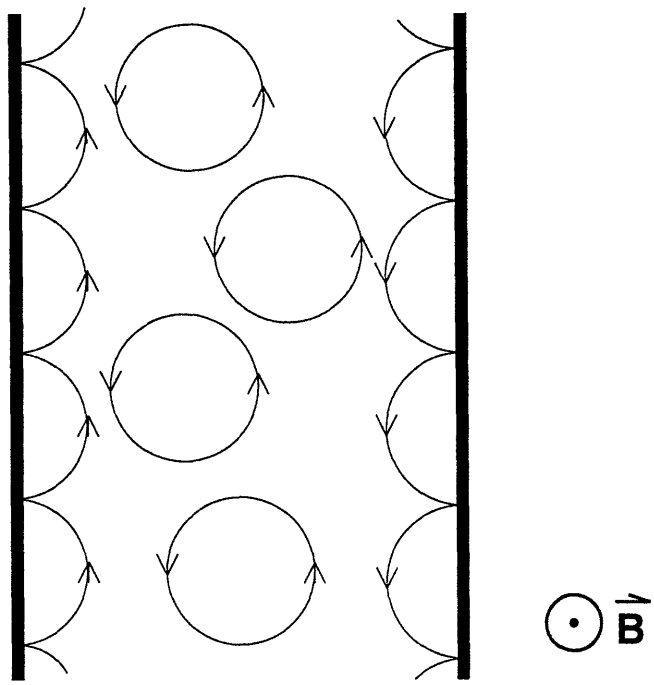

Figure 2-6: Illustration of interior and skipping orbits for a 2DEG with edges in the quantum Hall regime.

This equation can be used to calculated n_s from the period of experimental conductance data for a 2D mesa.

2.3 1D Regime

In this section we consider the impact of magnetic field on the 1D regime of a waveguide. By definition of the 1D regime, we are only concerned with the situation in which the electrons are coherent inside the device. We find, as in the 2D regime, that there are three magnetic field regimes. They are known as: low-field regime (cyclotron radius larger than the width of the waveguide), magnetic depopulation regime (cyclotron radius on the order of the width of the waveguide), and quantum hall regime (cyclotron radius much smaller than the width of the waveguide). These three regimes do not coincide with the three regimes for the 2D case. We discuss the conductance behavior in zero field and explore how it changes in the three magnetic field regimes.

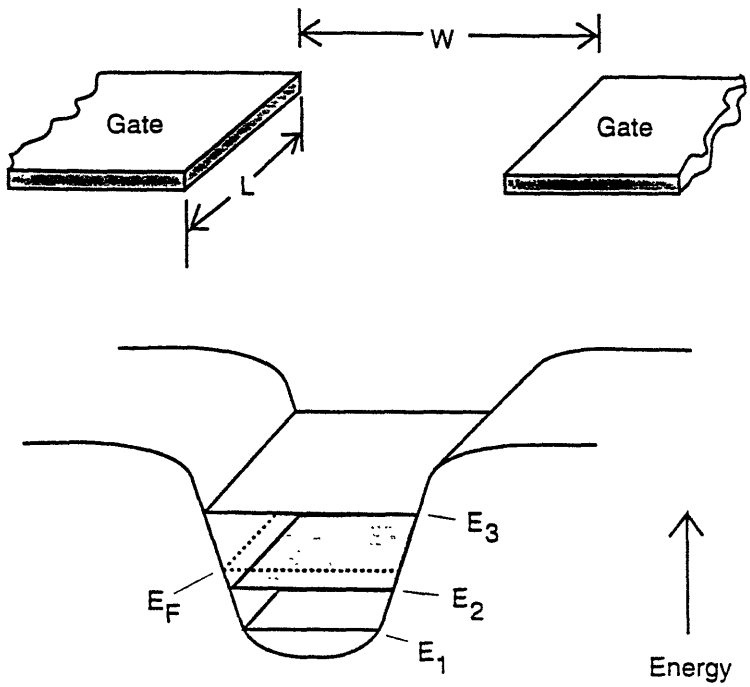

Figure 2-7: Illustration of energy levels for 1D subbands in an electron waveguide.[3]

2.3.1 Zero-field Regime

Current in a split-gate waveguide is dominated by transport across the 1D bottleneck between the source and drain because it has a much higher resistance than the 2DEG that contacts the waveguide. Thus, the two-terminal source-drain conductance is dominated by the conductance of the waveguide.

Electron motion in the waveguide is forbidden in two directions, so 1D subbands form as shown in Fig. 2-7. Each of the occupied subbands contributes to the conductance of the waveguide. To show that the conductance is quantized we must consider the 1D density of states that are moving in the positive direction ($k_x > 0$) for one subband, g_{1D}, and the electron velocity, v:

$$g_{1D}\left(k_x > 0\right) = \frac{1}{\pi}\frac{dk_x}{dE} \tag{2.18}$$

$$v\left(k_x\right) = \frac{1}{\hbar}\frac{dE}{dk_x}. \tag{2.19}$$

The current contributed by a single subband between source and drain when a voltage,

V_{ds} is applied is:

$$I = e\int_{-\infty}^{+\infty} g_{1D}\left(k_x > 0\right) v\left(k_x\right)\left[f\left(E\right) - f\left(E + eV_{ds}\right)\right] dE, \tag{2.20}$$

where f is the Fermi function. The product of the density of states and the velocity does not have any energy dependence and, if the low temperature approximation to the Fermi function can be made, Eq. 2.20 reduces to:

$$I = \frac{2e^2}{h} V_{ds}. \tag{2.21}$$

Each occupied subband therefore contributes $\frac{2e^2}{h}$ to the conductance. If there are n occupied subbands, the conductance is given by:

$$G = \sum_{i=1}^{n} \frac{2e^2}{h} = n\frac{2e^2}{h}. \tag{2.22}$$

The number of occupied modes is controlled by the width of the waveguide, which is modulated by the split-gate voltage, V_g. Reducing V_g narrows the waveguide, thereby causing the subbands to move up in energy, with successive subbands passing through the Fermi level and becoming depopulated. Therefore, as the gate voltage is made more negative in the 1D region, subbands are swept through the Fermi level and conductance plateaus are seen in V_g, as shown in Fig. 2-8.[3]

In Fig. 2-8, the steps are not infinitely sharp, as Eq. 2.22 suggests they should be. The softness of the steps is due to finite temperature and finite V_{ds}, which is taken into account by a convolution of Eq. 2.22 with an eV_{ds} window of energy and the thermal smearing of the Fermi function.[18] Other sources of conductance degradation will be discussed when the experimental data is considered in Chapter 4.

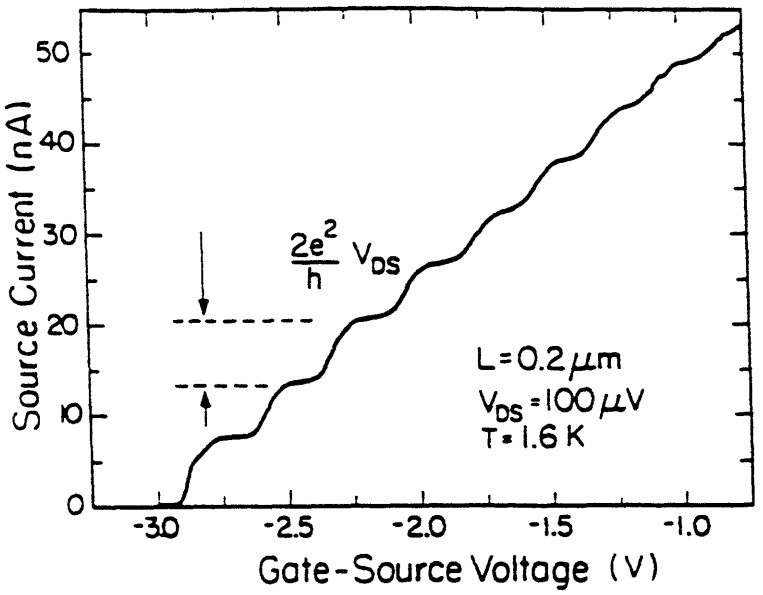

Figure 2-8: Quantized conductance for an electron waveguide in the 1D region.[3]

2.3.2 Low-field Regime

In the 1D region, the electrostatic potential contributes an extra term to the Hamiltonian in Eq. 2.4:

$$\mathcal{H} = \frac{(\mathbf{p} + e\mathbf{A})^2}{2m^*} + V(y), \tag{2.23}$$

where $V(y)$ is the electrostatic potential across the waveguide (the x-direction is along the waveguide). Clearly, for small fields, the electrostatic potential dominates and the magnetic field contribution to the Hamiltonian is negligible, while for high fields, the magnetic field term is dominant and the electrostatic potential term is negligible. The point at which these limiting approximations can be made depends on the strength and form of the electrostatic potential. We find that we can express the conditions for low-field, medium-field, and high-field regimes either in terms of width of the waveguide and the cyclotron radius (l_{cyc}) or the strength of the confining electrostatic potential and the strength of the magnetic field.

We define the *low-field regime* to be the regime in which the magnetic field confinement is negligible. By definition, in this regime the magnetic field has no effect

on the gate voltage dependence of the 1D conductance steps. The issue of interest is the relationship between the transition point from the low-field to the magnetic depopulation regime (in which the magnetic field depopulates the 1D subbands, as discussed in the next subsection), the strength and form of the electrostatic potential, and the waveguide's physical parameters. We examine this relationship for a simple electrostatic potential that results in an analytical solution and attempt to make some general conclusions.

The electrostatic confining potential due to the split-gate is often approximated by a parabolic potential[12] $V(y) = \frac{1}{2}m^*\omega_0^2 y^2$. Substituting this into the Hamiltonian from Eq. 2.23 yields the energy eigenvalues:

$$E_n = \left(n + \frac{1}{2}\right)\hbar\omega + \frac{\hbar^2 k_x^2}{2M}, \quad n = 0, 1, 2, ..., \tag{2.24}$$

where $\omega = \sqrt{\omega_c{}^2 + \omega_0{}^2}$ and $M = m^* \frac{\omega^2}{\omega_0{}^2}$. Clearly, the magnetic confinement is negligible if $\omega_0 \gg \omega_c$. Rewriting this low-field condition in terms of the cyclotron radius and a characteristic width of the electrostatic potential, $W = 2\hbar k_F / m^* \omega_0$, yields $l_{cyc} \gg W/2$. The characteristic width, W, is the spatial width of the potential at $V(y) = E_F$ and therefore represents the width of the waveguide. The critical field, $B_{crit} = 2\hbar k_F / eW$, is defined as the field at which $l_{cyc} = W/2$ or the field at which a cyclotron orbit fits perfectly inside the 1D waveguide.

A flat-bottomed potential with parabolic sides[11,10] has been offered as a more accurate approximation for the real electrostatic potential, but solutions for this potentials are not analytic. In addition, the exact relationship between the gate voltage and the confining potential is complex for any potential shape. Therefore, it is very difficult to draw anything but qualitative conclusions about the boundaries of the three magnetic regimes. The boundaries of the regimes are dependent on gate voltage, and we qualitatively expect the boundaries to shift to higher magnetic field as gate voltage is decreased and the electrostatic confinement becomes stronger.

Finally, it is important to note that although a low magnetic field does not change the gate voltage dependence of the conductance steps, it does affect the accuracy of

quantization. It has been shown that a magnetic field decreases the backscattering from a 1D constriction in a 2DEG.[22] This leads to a reduction of series resistance due to the transition from the wide 2DEG to the narrow 1D channel. Series resistance degrades the quality of quantization, so we expect to see more accurate quantization as the magnetic field is increased . This effect becomes increasingly apparent and saturates when the magnetic field is so strong that the electrostatic confining potential becomes negligible.

2.3.3 Magnetic Depopulation Regime

We define the onset of the magnetic depopulation regime to be where the magnetic confinement becomes comparable to the electrostatic confinement that defines the waveguide. This is equivalent to the cyclotron radius being on the order of some characteristic width of the waveguide, as discussed above. As in the previous subsection, we consider the parabolic approximation for the electrostatic potential and use the results to make some general conclusions about conductance behavior in the magnetic depopulation regime.

The energy eigenvalue equation for this system, Eq. 2.24 yields:

$$n = Integer\left[\frac{E_F}{\hbar\omega} - \frac{1}{2}\right], \tag{2.25}$$

We can see that, in this regime, for a given E_F and ω_0, the number of occupied modes is smaller than in the zero-field regime and decreases with increasing B. Therefore, for a given gate voltage, we expect the number of occupied modes and hence the conductance to drop as the magnetic field is increased. This is called *magnetic depopulation of 1D subbands.*[5,9] Eq. 2.25 also implies that, for increasingly larger magnetic fields, larger changes in E_F are needed to change n. This means the conductance steps in V_g get wider when the magnetic field is increased.

Although Eq. 2.25 is only valid for a parabolic potential, which may or may not be a good description of the actual electrostatic potential, the qualitative statements are valid for more realistic potentials. To see why this is true, we must consider

the qualitative effects of the magnetic field on the 1D subbands. A magnetic field provides additional confinement which tends to transform the density of states from 1D (characteristic of waveguide) to 0D (characteristic of Landau levels). In the region where the density of states is neither 1D or 0D, the total confinement due to both the magnetic field and the electrostatic potential is stronger than the confinement due to the electrostatic potential alone. Therefore, the subbands spread out, getting further and further apart and moving up through the Fermi level as the magnetic field is increased. Fewer of these subbands are occupied for a given gate voltage and a greater change in gate voltage is necessary to depopulate a subband. These trends should be present regardless of the exact form and strength of the electrostatic potential and its functional relationship to gate voltage.

2.3.4 Quantum Hall Regime

As discussed above, in the quantum Hall regime, the cyclotron radius is much smaller than the width of the waveguide, so the electrons are trapped in orbits that are much smaller than the waveguide. The magnetic confinement dominates and the electrostatic confinement can be neglected. The density of states is 0D, as in a large 2DEG at high field, and the conductance takes place entirely through edge states. The conductance characteristics are the same as the quantum Hall regime conductance characteristics as described by Eqs. 2.15, 2.16, and 2.17. In the plot of conductance versus gate voltage, we do not expect to see the dramatic change in slope that marks the transition between the 2D and 1D regimes at zero magnetic field.

2.4 Transition from 2D to 1D

In Section 2.2, we considered the strictly 2D regime, when the split-gate voltage is zero and the 2DEG is uniform over the entire mesa. As the gate voltage is lowered and the electron gas is depleted under the gates the conductance behavior becomes more complex. The electron concentration is no longer uniform over the entire mesa since it changes with gate voltage underneath the gates. The geometry factor in Eq. 2.3 and

the mixing of the longitudinal and transverse components of the magnetoconductance as discussed in Section 2.2.2 also will vary with gate voltage. It is therefore difficult to determine the conductance behavior in this transitional regime.

2.5 Summary

In this chapter, we studied the physics of transport in a split-gate electron waveguide as a function of magnetic field and gate voltage to derive conductance characteristics. We found that there are two gate voltage regimes, the 2D and 1D regimes. In the 2D regime, there are three magnetic field regimes: the low-field classical Hall regime, the high-field classical Hall regime, and the quantum Hall regime. In the low-field classical Hall regime, the cyclotron radius is much larger than the mean free path of electrons and the energy spacing of the Landau levels is much smaller than the thermal smearing of the Fermi function. In the high-field classical Hall regime, the cyclotron radius is much smaller than the mean free path but the Landau level spacing is still smaller than thermal smearing. In the quantum Hall regime, the Landau level spacing is much greater than the thermal smearing. There are also three magnetic field regimes in the 1D regime: the low-field regime, the magnetic depopulation regime, and the quantum Hall regime. The cyclotron radius is much larger than the width of the waveguide in the low-field regime, comparable to the width of the waveguide in the magnetic depopulation regime, and much smaller than the width of the waveguide in the quantum Hall regime. The transport characteristics of an electron waveguide in a magnetic field will be a strong function of the magnetic field.

Chapter 3

Experimental Data

3.1 Introduction

We have performed measurements of magnetoconductance in split-gate electron waveguides. In one set of experiments, we study the gate-voltage dependence of conductance at various magnetic field values. In the other set, we examine the magnetic-field dependence of conductance at various gate voltages in the 2D and 1D regions. In this chapter we describe our experiments and present the experimental data, noting and discussing the important features.

3.2 Device Description and Experimental Technique

The electron waveguide we measure was fabricated on an AlGaAs/GaAs modulation-doped heterostructure that was grown by MBE by M.R. Melloch at Purdue University.[2] A cross-section of the heterostructure is show in Fig. 3-1. As grown, the sample had an electron mobility of 1.24×10^6 cm^2/Vs and 2DEG electron concentration of 4.3×10^{11} cm^{-2} at 4.2 K.[23] The device was fabricated by C.C. Eugster at Massachusetts Institute of Technology as described in reference 1. Electron-beam lithography of the fine features was performed by M.J. Rooks at Cornell University.[24] After fabrication,

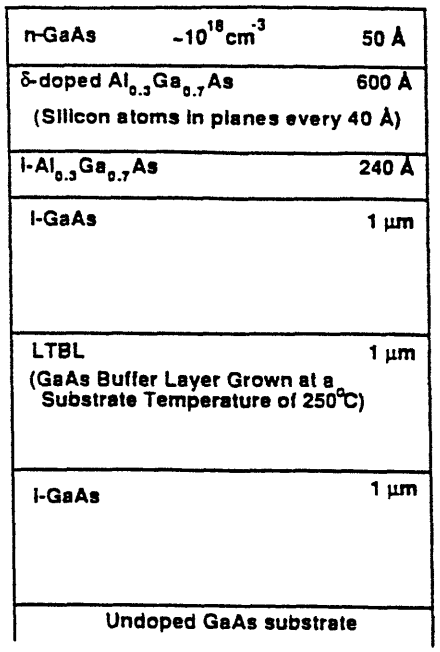

Figure 3-1: Cross-section of AlGaAs/GaAs heterostructure[3].

electron mobility and concentration in the 2DEG were measured at 1.6 K using a van der Pauw structure. The obtained values were $1.2 \times 10^6\ cm^2/Vs$ and $3.8 \times 10^{11}\ cm^{-2}$, respectively, in excellent agreement with as-grown measurements.

The layout of the mesa, gates, and contacts of a typical device is shown in Fig. 3-2. The mesa is $32\mu m \times 28\mu m$ in its central region. The lithographic gate width and length of the device we have studied, the center one, are 0.35 μm and 0.5 μm respectively. The bottom left ohmic contact is used as the drain and the top right ohmic as the source.

We use a lockin measurement technique in our experiments because voltages and currents are very small. The schematic of the measurement setup is shown in Fig. 3-3. An AC voltage of 110 mV at 19 Hz is applied by a Princeton Applied Research 5210 Lockin Amplifier through a 1/1100 voltage divider that reduces the voltage to 100 μV to the drain of the electron waveguide. The source AC current is measured through the current preamplifier of the lockin, which outputs a DC voltage proportional to the AC current. The lockin output is monitored by an HP 4145B Semiconductor Parameter Analyzer, which also controls the side gate voltages. Conductance is computed

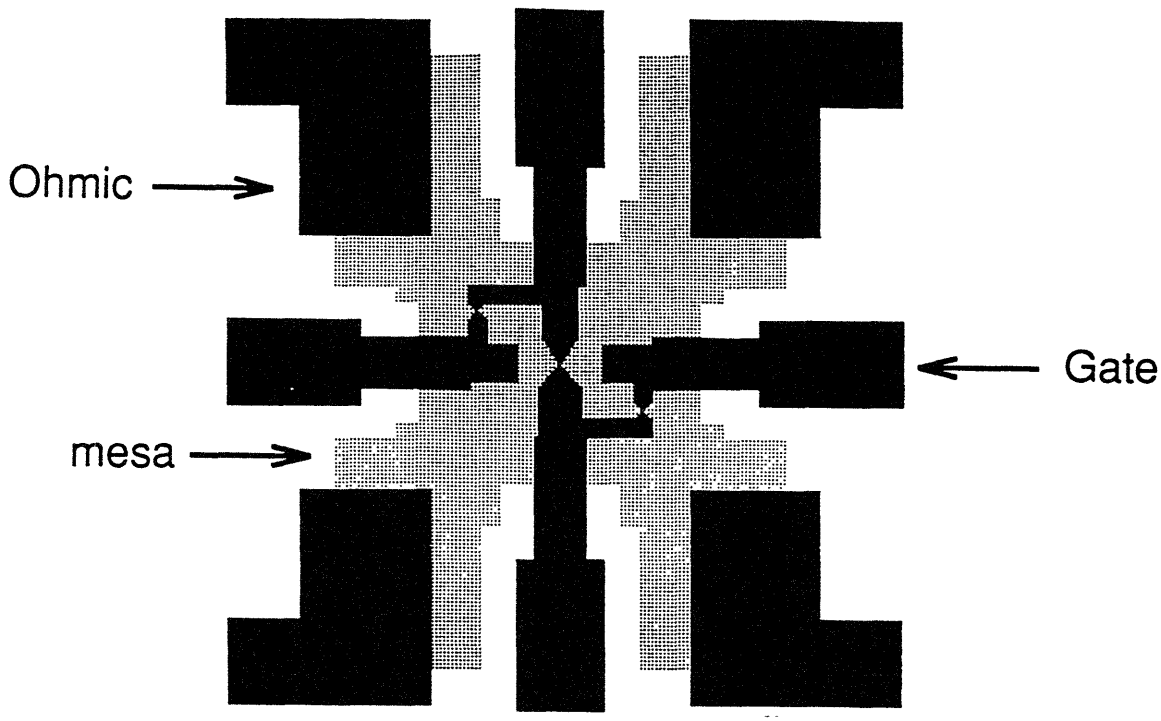

Figure 3-2: Mesa layout of electron waveguide.

by dividing the source current (lockin output multiplied by an appropriate proportionality constant) by the input voltage (100 μV). In all experiments, the bottom gate in Fig. 3-2 is fixed at -0.9 V (below V_{th}^{2D}) and the top gate is varied between 0 V and V_{th}^{1D}. For the device measured, V_{th}^{2D} is approximately -0.5 V and V_{th}^{1D} ranges from about -1.2 V to -1.7 V.

Measurements are made in a Janis cryostat at 1.6 K. Low temperatures are necessary to reduce the thermal smearing so that individual modes are resolvable. The magnetic field is applied by a 9 Tesla superconducting magnet powered by a Lakeshore 612 Superconducting Magnet Power Supply and controlled by a Lakeshore 601 Magnet Control Unit.

3.3 Experimental Results and Discussion

Two sets of experiments were carried out. In the first set, the top gate is continuously swept from 0 V to V_{th}^{1D} at discrete magnetic field values from 0 T to 9 T. In the second set, the magnetic field is continuously swept from 0 T to 9 T for discrete

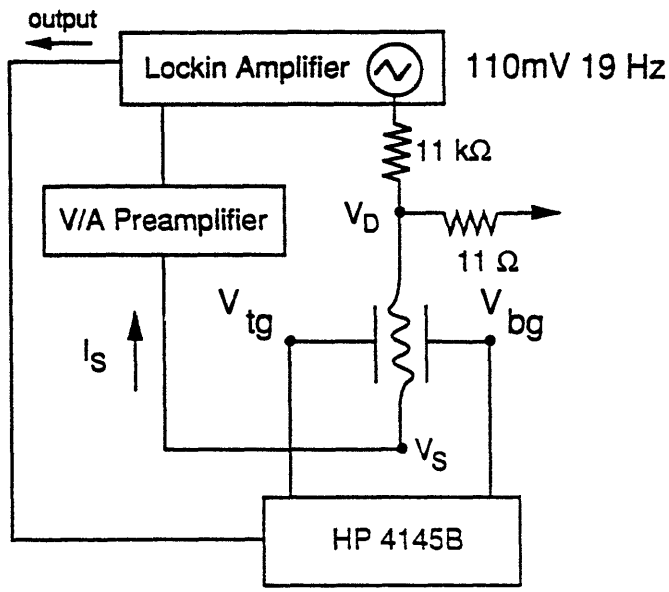

Figure 3-3: Measurement setup schematic.[3] Wavy line represents waveguide.

top-gate voltages from 0 V to V_{th}^{1D}. In both experiments, the bottom gate voltage is kept at -0.9 V. We present below the results for each set of experiments and note the important features.

3.3.1 Conductance Versus Top-Gate Voltage for Discrete Magnetic Field Values

To observe the effect of a magnetic field on the quantized conductance steps, we measure conductance versus top-gate voltage at discrete values of magnetic field. As is typically observed in these kinds of devices,[3] both the 1D and 2D threshold voltages vary between experimental runs due to different conditions during cool-down to 1.6 K. We present data from three experimental runs carried out on different dates that exhibit different threshold voltages. Conductance, in units of $\frac{2e^2}{h}$, versus gate voltage curves at zero magnetic field for each run are shown in Fig. 3-4. The inset magnifies the end of the 1D tail.

The conductance curves in Fig. 3-4 exhibit a 2D region and a clear 1D tail. Although the 2D threshold voltages do not vary appreciably, the 1D threshold voltages

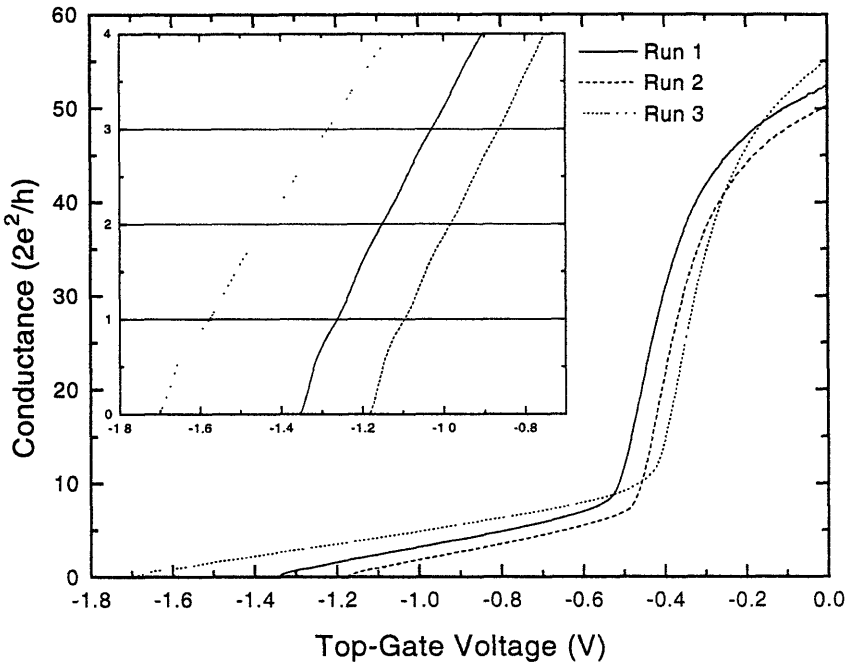

Figure 3-4: Conductance versus top-gate voltage with zero magnetic field for three experimental runs. The inset shows the quantized conductance steps in the 1D region.

are very different from run to run. As mentioned above, the threshold shifts are due to different cool-down conditions. More or fewer electrons may be frozen into or freed from traps as the temperature is lowered, thereby shifting threshold voltages.[3]

The inset to Fig. 3-4 shows two or three rather indistinct quantized conductance steps at the end of the 1D tail for each run. The softness of the steps is due partly to thermal and voltage window smearing, and partly to non-idealities in the device such as impurities and surface states.

In each run, we sweep the gate voltage at various discrete values of magnetic field. The first run is shown in Fig. 3-5, the second in Fig. 3-6, and the third in Fig. 3-7. The curves are plotted on a semilog scale to show the whole range of conductance values. For each of these runs, the 1D threshold voltage varies slightly with magnetic field in what appears to be a random way. The relatively large shift in threshold during the first run as evident in Fig. 3-5 is possibly due to a sudden temperature spike that freed electrons from traps.

Threshold considerations aside, the qualitative characteristics from run to run are

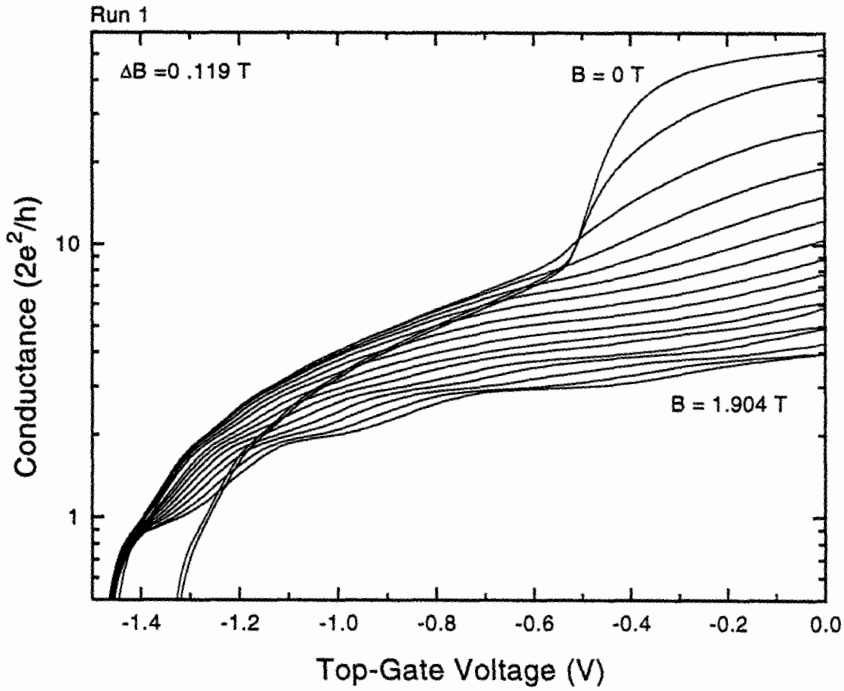

Figure 3-5: Conductance versus top-gate voltage for the first experimental run.

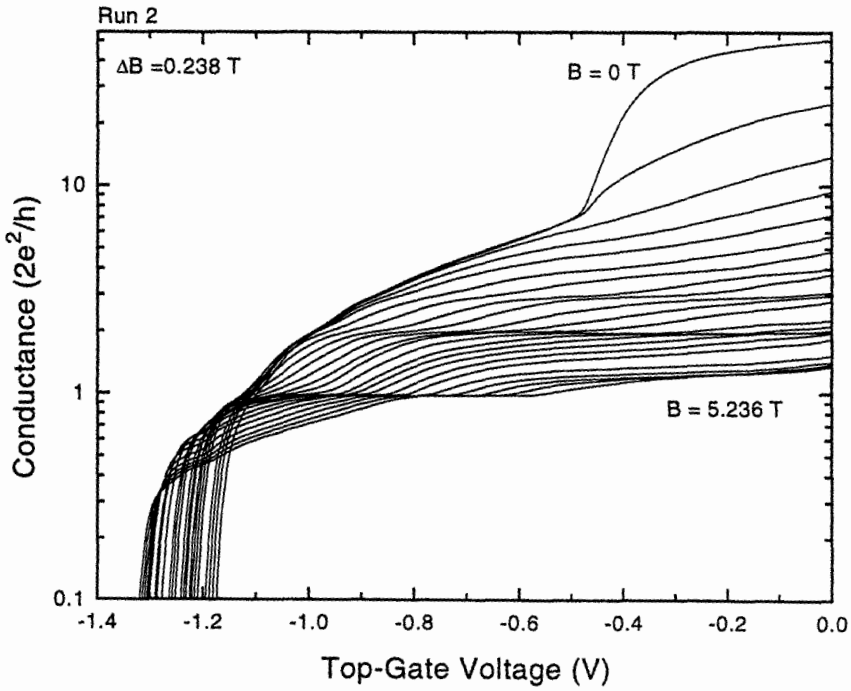

Figure 3-6: Conductance versus top-gate voltage for the second experimental run.

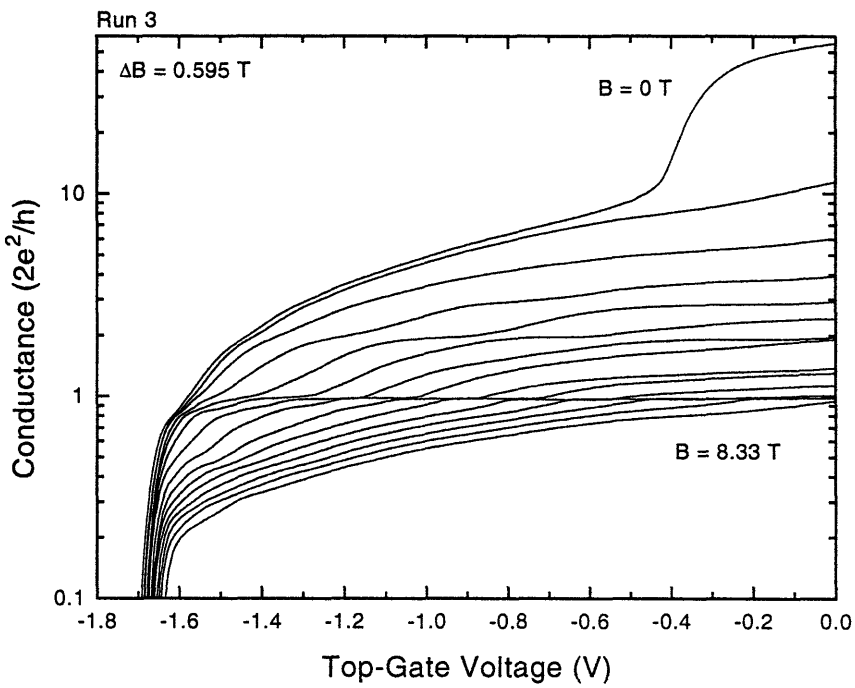

Figure 3-7: Conductance versus top-gate voltage for the third experimental run.

the same. As the field is increased, the conductance in the 2D regime drops until it becomes quantized. The drop in conduction with magnetic field is best seen in Fig. 3-5 and the quantization is best seen at higher fields as in Figs. 3-6 and 3-7. In the 1D regime, the quantized conductance steps are not affected by low fields as shown in the first curves of Figs. 3-5 and 3-6, where for high fields the traces tend to cluster at integer values of $\frac{2e^2}{h}$. As the field is increased above $B \simeq 0.5\ T$, the 1D steps become wider and flatter. In the high-field quantum Hall limit, both the 1D and 2D regions are quantized and conductance steps extend over the entire gate-voltage range. In this quantum Hall regime, the steps continue to widen as the field is increased, leading to fewer steps at a given magnetic field value. In the highest magnetic field traces of Fig. 3-7 there is only one quantized conductance step. At very high fields, there seems to be another step at $\frac{1}{2}\frac{2e^2}{h}$. This implies that the field is high enough to lift the spin degeneracy as discussed in Chapter 4.

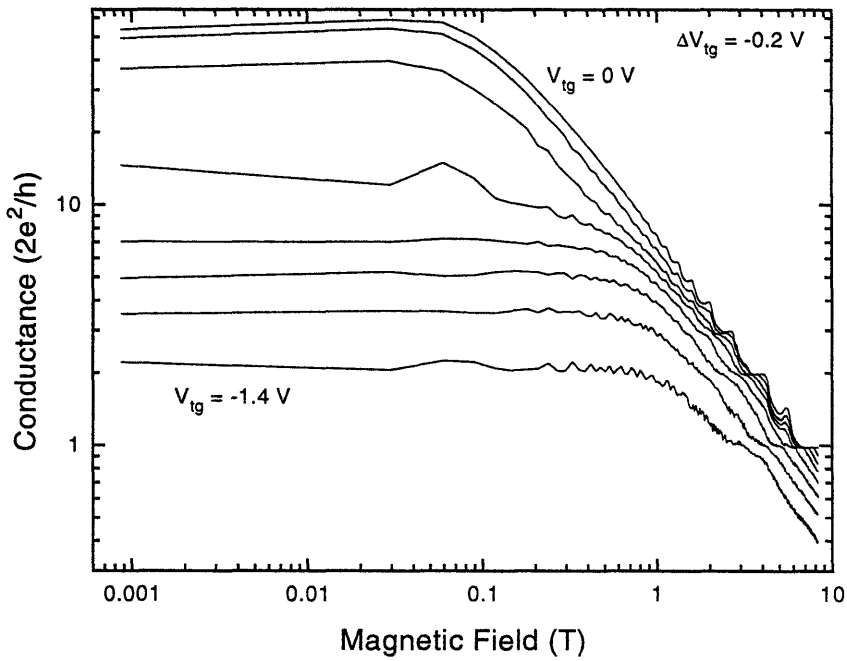

Figure 3-8: Conductance versus magnetic field for various top-gate voltages.

3.3.2 Conductance Versus Magnetic Field for Discrete Top Gate Voltages

To further explore the magnetic field regimes discussed in Chapter 2, we measure conductance versus magnetic field at discrete top-gate voltages that range from the 2D to 1D regime. As in the previous set of experiments, we expect measurements to vary somewhat from run to run, but in this case we only performed one set of measurements. Conductance versus magnetic field is plotted on a log-log scale in Fig. 3-8. The top four traces (V_{tg} = 0, -0.2, -0.4, and -0.6 V) are in the 2D regime, and the bottom four (V_{tg} = -0.8, -1.0, -1.2, and -1.4 V) are in the 1D regime.

In the 2D regime, the conductance is constant at low fields and begins to fall off as $1/B$ when $B \simeq 0.1\ T$. The previous set of experiments does not show this regime of constant conductance because the step in magnetic field is too large. At fields above $B \simeq 0.5\ T$, the conductance begins to oscillate and then exhibits clearly defined plateaus at integer values of $\frac{2e^2}{h}$. We notice a slight dip in the plateaus that is less prominent at higher fields. We also see that there is a feature at $\frac{3}{2}\frac{2e^2}{h}$. As mentioned above, this step is due to spin-splitting. The conductance in the 1D regime remains

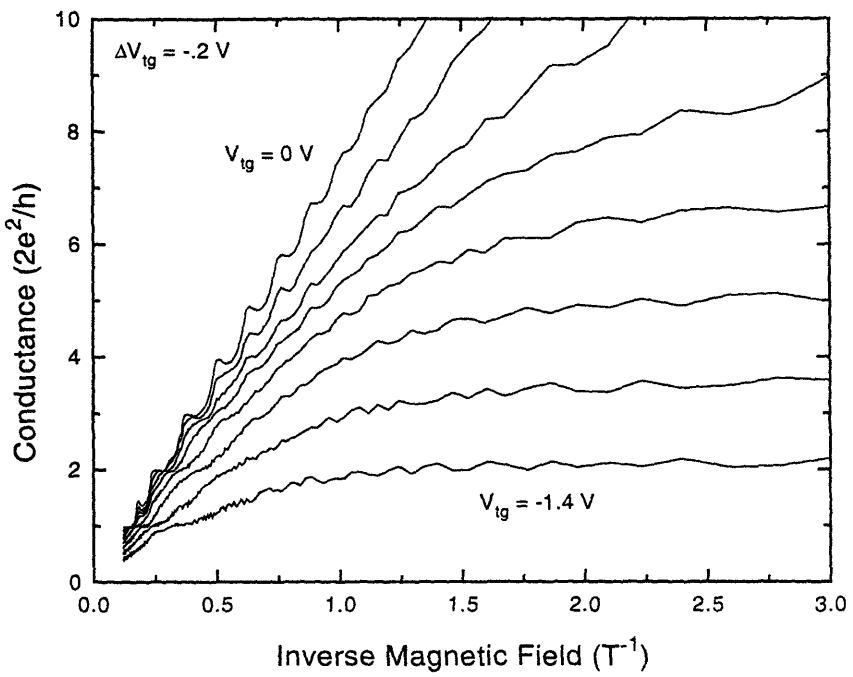

Figure 3-9: Conductance versus inverse magnetic field for various top-gate voltages.

constant to higher fields ($B \simeq 0.5\ T$), but it eventually decreases also as $1/B$. In the high-field limit, all of the conductance curves decrease with increasing field and show quantized conductance steps.

It is interesting to examine the high-field regime in more detail. A linear plot of conductance versus inverse magnetic field for high fields is shown in Fig. 3-9. For all gate voltages, the conductance plateaus in the high-field limit are periodic in $1/B$ with a gate-voltage dependent period. All magnetic field features in the 2D and 1D regimes will be examined in more detail in Chapter 4.

3.4 Summary

We have carried out measurements of conductance in a split-gate electron waveguide as a function of split-gate voltage and magnetic field. The 2D conductance is constant for low fields, then begins to fall off as $1/B$ as the magnetic field is increased. At higher fields, the conductance shows periodic behavior in magnetic field and becomes quantized in magnetic field at integer values of $\frac{2e^2}{h}$. The 1D conductance is constant

for low fields and then begins to fall off as $1/B$ also. Therefore, the 1D quantized conductance steps in gate voltage are unaffected by low fields but eventually widen and flatten at higher fields.

Chapter 4

Comparison of Simulated, Experimental, and Theoretical Data

4.1 Introduction

In this chapter we compare simulated, experimental and theoretical results. In the first section we describe the methods used to simulate an electron waveguide and compute the conductance and present the simulated data for a typical waveguide. In the second section we discuss and compare the simulated, experimental, and theoretical data in the context of the three magnetic field regimes defined in Chapter 2.

4.2 Zero-field Simulation of Electron Waveguides

As discussed in Chapter 2, the magnetic behavior of a waveguide depends upon the interaction between the electrostatic potential that defines the waveguide and the magnetic field. For the purposes of magnetic depopulation, the electrostatic potential of a waveguide is often modeled as a parabolic well[12] or a square well.[9] More complicated models such as a flat-bottomed well with parabolic sides have also been used,[11,10] but these models have more parameters and do not yield analytical

solutions.

To determine if we can reasonably model the electrostatic potential in the device we measure as either a parabolic or a square well, we simulate an electron waveguide using a computer program developed by G.L. Snider that self-consistently solves Poisson's equation and Schrodinger's equation in two dimensions.[14] In this section, we discuss the methods used to match the simulation parameters with measurable device characteristics and incorporate thermal and voltage smearing. We present and discuss the resulting simulated conductance. Finally, we examine the shape of the simulated electrostatic potential.

4.2.1 Fitting Parameters

Device measurements yield values for V_{th}^{2D}, V_{th}^{1D}, and $n_s\,(V_{tg} = 0)$ at zero magnetic field. To simulate the device, dimensions and doping must be specified. In principle, knowledge of layer structure and device dimensions should be sufficient to model the electrostatics of a waveguide. In practice, some of the simulation parameters must be adjusted for the simulation to yield the measured V_{th}^{2D}, V_{th}^{1D}, and $n_s\,(V_{tg} = 0)$. We describe the process of for fitting the simulation parameters so that the simulation can be used to match measured data.

As shown in Fig. 3-1, the insulator layer of the heterostructure is delta-doped. The delta doping is approximated in the simulation by layers with a finite thickness of 10 $\AA$, each with a constant dopant concentration that is adjusted so that the simulated $n_s\,(V_{tg} = 0)$ matches the measured $n_s\,(V_{tg} = 0)$ at 1.6 K. This procedure is reasonable because the actual doping is not well known and carrier freeze out at low temperatures is hard to model. In contrast, the layer thicknesses of the heterostructure are not adjusted in the simulation because they are very well known from MBE calibrations. This process yields a V_{th}^{2D} in excellent agreement with experiments, but V_{th}^{1D} becomes much too negative.

One study has shown that, for electron waveguides of finite length, there is a critical width below which there is no 1D behavior of the waveguide.[25] In addition, a positive shift of V_{th}^{1D} with gate length was observed.[25] These effects are attributed to

an effective extension of the gates due to interaction of the gates and surface states at the exposed GaAs surface neighboring the gates. This extension of the gates results in a decrease in the effective electrostatic width of the waveguide, which increases V_{th}^{1D}. It is reasonable to assume that this effect causes the measured V_{th}^{1D} to be more positive than the simulated V_{th}^{1D}.

To simulate the extended gates using the Poisson/Schrodinger solver the gates are widened, narrowing the split-gate width until the simulated V_{th}^{1D} agrees with the measured V_{th}^{1D}. To achieve the range of measured V_{th}^{1D}'s as shown in Fig. 3-4 the slit width must be narrowed from the actual width, 0.35 μm, to 0.175-0.22 μm. Thus the critical width appears to be 0.13-0.175 μm, which is consistent with observed critical widths of 0.2-0.25 μm in devices with 1 μm gate lengths.[25]

4.2.2 Thermal and Voltage Window Smearing

Once the simulation parameters have been chosen, the conductance may be computed from the simulation results. The Poisson/Schrodinger solver gives the energy of the subbands with respect to the Fermi level at a given top-gate voltage in the 1D region. As discussed in Chapter 2, each occupied subband of a waveguide contributes $\frac{2e^2}{h}$ to the conductance. Therefore, a plot of the number subbands below the Fermi level multiplied by $\frac{2e^2}{h}$ as a function of gate voltage yields ideal, infinitely sharp quantized conductance steps. The ideal conductance must be convolved with an eV_{ds} window of energy and the thermal smearing of the Fermi function to include the effects of finite V_{ds} and finite temperature, respectively.[18] Because the Poisson/Schrodinger solver calculates the energy of each subband for a given gate voltage, this convolution can be easily performed numerically.

4.2.3 Simulated Conductance

We present results for a simulated waveguide with V_{th}^{1D} equal to the average V_{th}^{1D} ($\simeq -1.41V$) from the three experimental runs presented in Chapter 3. The split-gate width used in the simulation for this case is 0.195 μm. The simulated conductance,

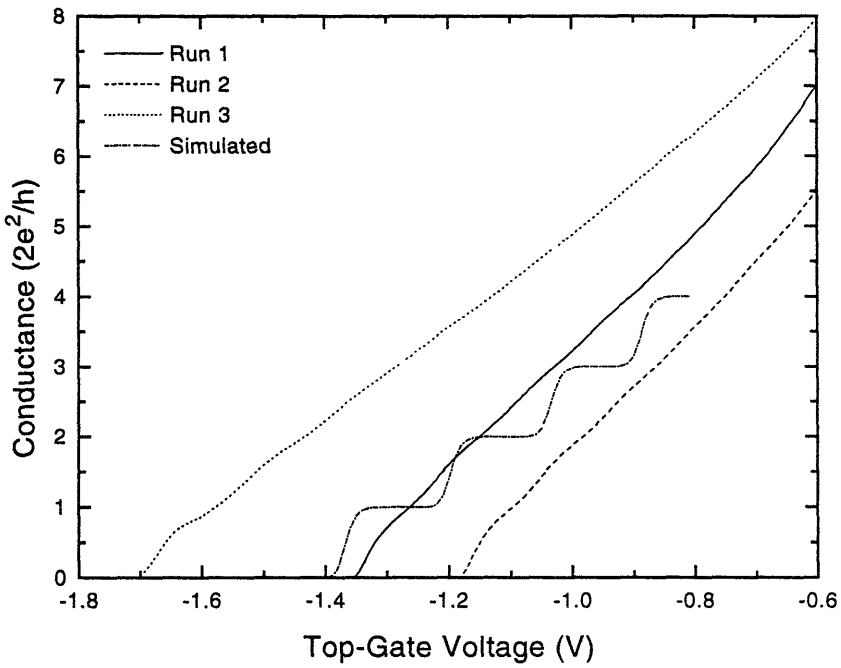

Figure 4-1: Simulated and experimental conductances versus top-gate voltage

as computed from the simulation results and including thermal and voltage window smearing effects as described in the previous subsection is plotted versus top-gate voltage in Fig. 4-1. Also plotted is the measured conductance for each of the three experimental runs. The simulated conductance curve clearly shows four well-defined, slightly rounded conductance steps. The simulated conductance steps are wider and more distinct than the steps in all three experimental runs. In addition, the slope of the envelope of the simulated steps is slightly shallower than the slope of all but the third run, which has a much more negative threshold voltage.

Inaccurate modeling of the interaction between the gates and surface states may account for some of the difference between the simulated and experimental data. For example, if the interaction is such that the electrostatic potential is weaker than simulated, the energy levels will be closer together and the steps will be more indistinct and narrower. Any nonidealities in the device such as impurities,[1] series resistance,[4,10] or tunneling[26] are also not included in the simulation and are known to degrade the measured quantization.

4.2.4 Examination of the Potential Shape

As discussed in Section 2.3.3, the shape of the electrostatic potential that defines the waveguide is the key to a quantitative analysis of the magnetic depopulation regime. With this in mind, we consider what simulation results predict for the potential shape.

The Poisson/Schrodinger solver calculates the position of the conduction band with respect to the Fermi level. In Fig. 4-2, a plot of $(E_F - E_C)$ versus distance across the waveguide at the AlGaAs/GaAs interface shows the electrostatic potential of the waveguide. The position of the split-gates are indicated by the shaded regions near the bottom horizontal axis and the inset zooms in on the gap between the gates. For the most positive gate voltages, the potential has a relatively flat bottom and the walls curve up. As the gate voltage is lowered closer to threshold, the bottom of the potential rises and becomes more parabolic. This suggests that the electrostatic potential could be reasonably approximated by a parabolic potential for gate voltages near threshold, but a more complicated potential is needed far above threshold. To obtain more quantitative information about the shape of the well, we consider the relative energies of the bottom of the subbands.

Both a parabolic well[12] ($V(y) = \frac{1}{2}m^*\omega_0{}^2y^2$) and an infinite square well[9] of width W_{sq} have been used to approximate the electrostatic potential of a waveguide. The energy levels for a parabolic and a square well are given by: $E_{para} = \left(n_{para} + \frac{1}{2}\right)\hbar\omega_0$ ($n_{para} = 0, 1, 2, \ldots$) and $E_{sq} = n_{sq}{}^2\pi^2\hbar^2/2m^*W_{sq}^2$ ($n_{sq} = 1, 2, 3, \ldots$). Because the width of the potential (ω_0 or W_{sq}) changes with gate voltage in a complex way, we must examine a quantity that does not depend on ω_0 or W_{sq}. It turns out that the energy difference between the second and third subbands $(E_3 - E_2)$ divided by the energy difference between the first and second subbands $(E_2 - E_1)$ is independent of ω_0 in the parabolic case and W_{sq} in the square well case. In Fig 4-3 this ratio is plotted versus gate voltage using the values of the energy levels from the self-consistent simulation results. This quantity is not defined below -1.03 V, where the third subband rises above the Fermi level and is cut off. Also plotted for comparison is the same ratio for square and parabolic wells. We see that the simulated structure has an energy spectrum that is not strongly dependent upon gate voltage and is more similar to a

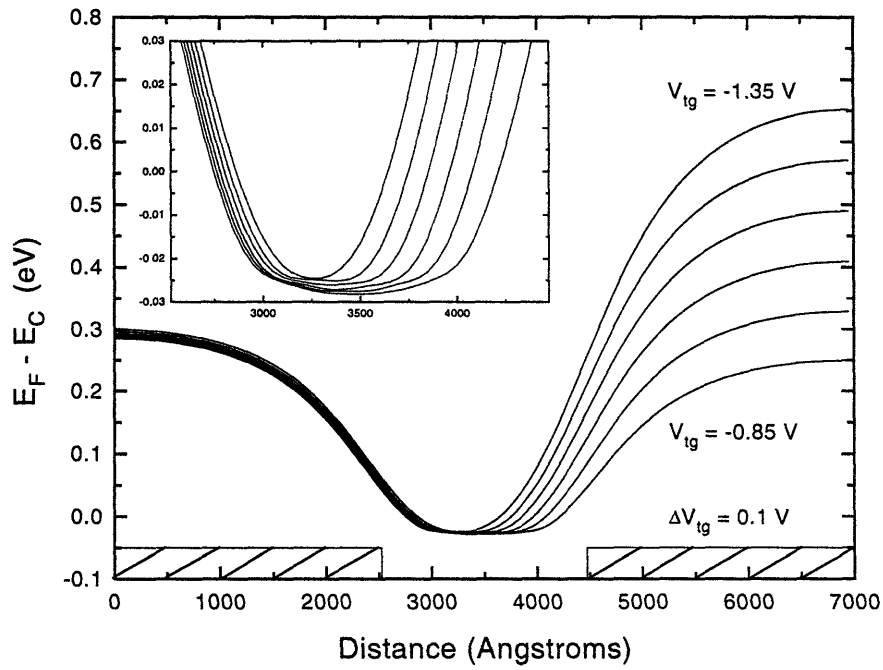

Figure 4-2: The electrostatic potential across the waveguide. The shaded regions show the position of the split-gate and the inset zooms in on the gap between the gates.

parabolic well than a square well over the range of gate voltages. This suggests that a parabolic well is a better approximation to the simulated potential than a square well, but a more realistic potential would need to include a flat-bottomed portion as well as non-infinite walls.

4.3 Discussion and Comparison of Simulated, Experimental, and Theoretical Data

In this section, we discuss and compare the simulated data, the experimental magnetoconductance data of Chapter 3, and the theoretical models discussed in Chapter 2. We consider the 2D and 1D regimes of the waveguide in turn, analyzing the important features in the data.

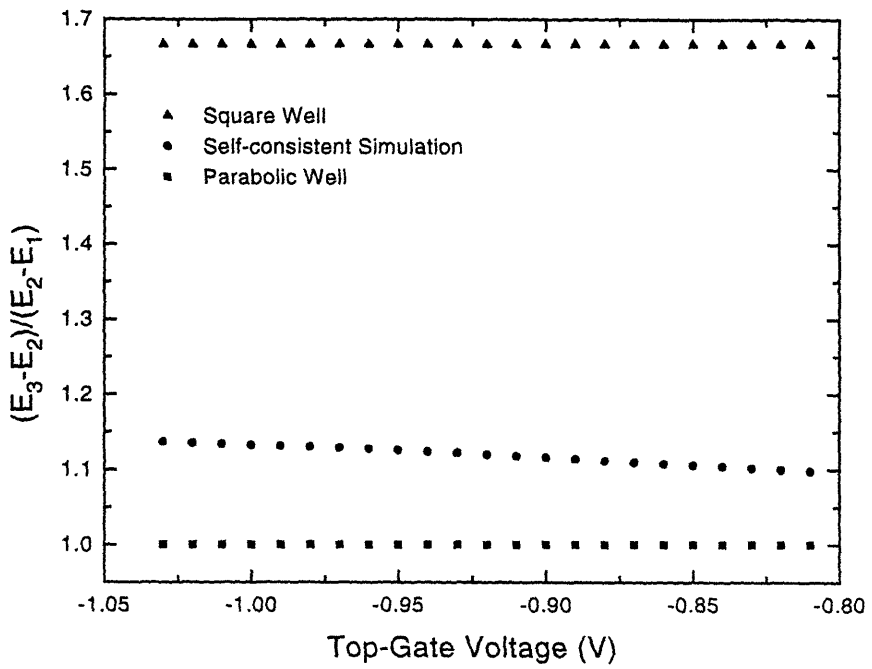

Figure 4-3: Energy difference between the second and third subband divided by the energy difference between the first and second subband for the simulated structure and parabolic and square wells versus top-gate voltage.

4.3.1 2D Regime

The theory of transport in the 2D regime was discussed in Section 2.2, where we considered only the strictly 2D case, for which the split-gate voltage is zero and the electron gas is uniform over the entire mesa. In the experimental setup, the bottom side of the split-gate as shown in Fig. 3-2 is fixed below the 2D threshold so that the 2DEG beneath it is depleted, and the voltage on the top side of the split-gate is varied. Although the 2DEG is depleted under the bottom gate, the 2DEG is uniform over the rest of the mesa when the top-gate voltage is zero and the theory presented in Section 2.2 applies.

As discussed in Section 2.2, we expect three magnetic field regimes in the 2D region. Fig. 3-8 clearly shows three field regimes for $V_{tg} = 0$. The conductance is nearly constant for low fields, begins to fall off at medium fields, and displays a sharp plateau structure at high fields. Next we look at these three regimes in more detail.

Low-field Classical Hall Regime

The two-terminal conductance in the low-field classical Hall regime is given by Eq. 2.3, which depends on a geometry factor, g, the 2D electron concentration, n_s, and the electron scattering time, τ. The scattering time is related to electron mobility by:

$$\tau = \frac{m^* \mu_e}{e}. \tag{4.1}$$

Therefore, the geometry factor, g is given by:

$$g = \frac{G(B=0)}{n_s e \mu_e}. \tag{4.2}$$

Using the values for n_s and μ_e obtained from van der Pauw measurements and the zero-field measured conductance from the second experiment, g is calculated to be 0.057. As discussed in Section 2.2.1, for a simple rectangular geometry, g is equal to W/L, which is simply the inverse of the number of squares of the mesa. Although the geometry of our mesa is not simple, as shown in Fig. 3-2, the calculated geometry factor seems reasonable given the relative dimensions of the mesa.

High-field Classical Hall Regime

In the high-field classical Hall regime, the conductance is a geometrical mix of the transverse and longitudinal conductivities. Eqs. 2.8 and 2.11 describe the conductivity for two extreme geometrical cases. Both of these equations apply to a simple rectangular mesa, but the shape of our mesa is rather irregular. This can be partly accounted for by the substitution of the geometrical factor, g, for W/L in Eqs. 2.8 and 2.11, which yields:

$$R_{2t} = G_{2t}^{-1} = \frac{1}{g}\rho_{xx} + \rho_{xy} \qquad (g \ll 1) \tag{4.3}$$

and

$$G_{2t} = g\sigma_{xx} + \sigma_{yx} \qquad (g \gg 1). \tag{4.4}$$

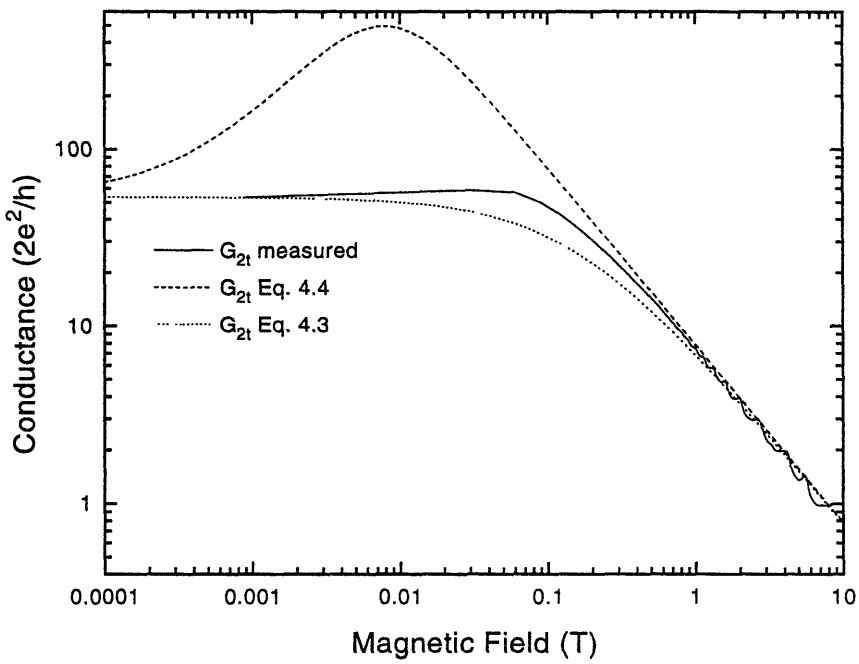

Figure 4-4: Measured and predicted conductance versus magnetic field for zero top-gate voltage.

Eqs. 4.3 and 4.4 are plotted together with the measured two-terminal conductance for zero top-gate voltage in Fig. 4-4. Eq. 4.3 is a good fit, which is reasonable given that $g \ll 1$. Eqs. 4.3, 2.9, and 2.10 predict a turning point or corner in the conductance when the magnetic field is given by:

$$B = \frac{m}{ge\tau} = \frac{1}{g\tau}. \tag{4.5}$$

Using the mobility obtained from van der Pauw measurements and the geometry factor calculated above, the theoretically calculated turning point is found to be 0.15 T, in excellent agreement with experiment. The imperfect fit of Eq. 4.3 suggests there is more complicated geometry mixing than is described by the equation, as expected for an irregular mesa.

Quantum Hall Regime

As discussed in Section 2.2.3, the conductance begins to show periodic structure when the spacing of the Landau levels ($\hbar\omega_c$) becomes greater than the thermal smearing of

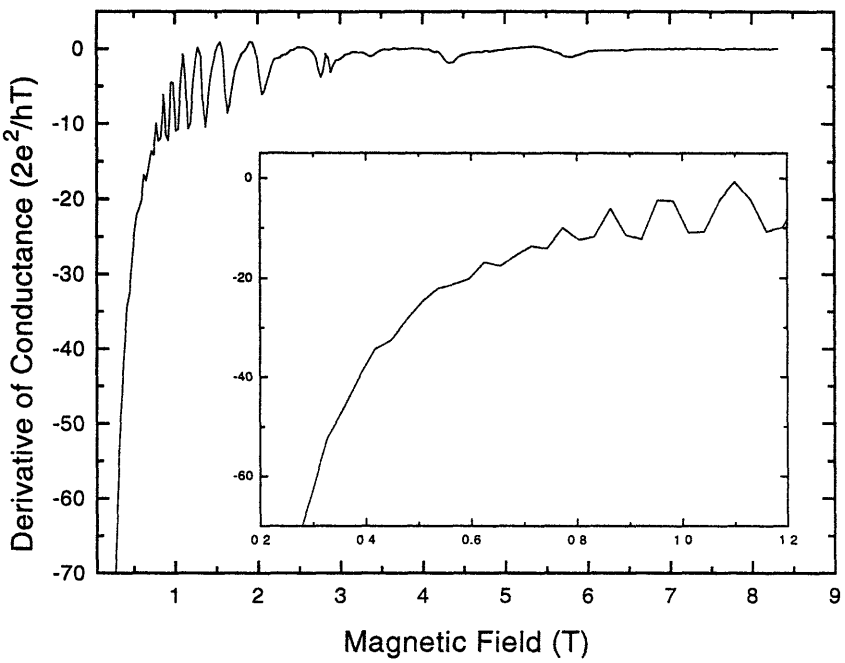

Figure 4-5: Derivative of conductance versus magnetic field for $V_{tg} = 0V$. Inset details onset of oscillations.

the Fermi function ($3.5kT$). The threshold magnetic field can be calculated theoretically by equating the Landau level separation with the thermal smearing and solving for the magnetic field. At 1.6 K, the theoretical threshold field is found to be 0.28 T. The threshold field can be experimentally extracted by examining the derivative of the conductance with respect to magnetic field as shown in Fig. 4-5. This graph shows oscillations where the conductance displays plateaus. A periodic structure begins to appear near $B \simeq 0.5\ T$, in reasonable agreement with theory. The difference between experiment and theory may be due to broadening of Landau levels caused by scattering.[6]

The theory presented in Section 2.2.3 predicts the conductance in the quantum Hall limit to be quantized at integral values of $\frac{2e^2}{h}$. The conductance quantization is clearly evident in Fig 3-8. The dips in conductance between plateaus are most likely due to scattering between edge states on opposite sides of the mesa. At higher fields, the number of occupied edge states decreases and the edge states become further apart, so the probability of scattering between edge states decreases and the steps are flatter and better quantized.

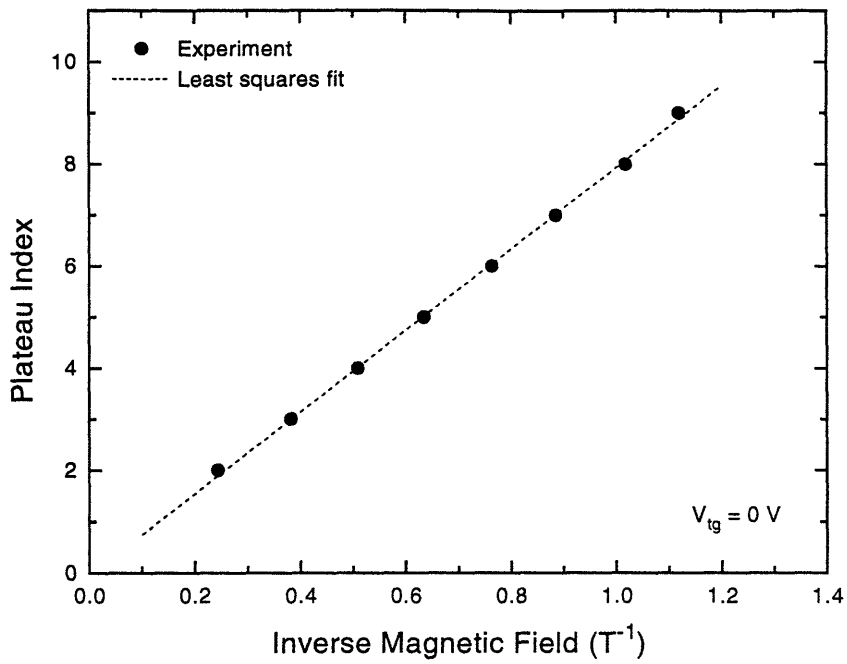

Figure 4-6: Plateau index versus inverse magnetic field at the onset of each plateau for zero top-gate voltage.

Theory also predicts the conductance plateaus to be periodic in $1/B$ with a period that is proportional to $1/n_s$, as expressed by Eq. 2.17. Therefore, a plot of plateau index versus inverse magnetic field for the onset of each plateau should be a straight line that passes through the origin with a slope equal to $n_s h/2e$. In this manner, n_s can be extracted from experimental data for gate voltages in the 2D regime.

Plateau index as a function of inverse magnetic field at the onset of each plateau for zero top-gate voltage is plotted in Fig. 4-6. The points lie on a straight line that crosses the origin. n_s calculated from the slope of this line is $3.9 \times 10^{11} cm^{-2}$, in excellent agreement with van der Pauw measurements, which yield $n_s = 3.8 \times 10^{11} cm^{-2}$.

n_s is extracted from experimental data for other gate voltages in the 2D regime and plotted together with n_s as computed by the Poisson/Schrodinger solver in Fig. 4-7. The simulated n_s falls much more rapidly with decreasing gate voltage than the experimental n_s does. This is easily explained by the edge channel model of the quantum Hall effect.[21,27] As the top-gate voltage is lowered and the electrons under the top gate are depleted, the highest Landau level edge channel is not supported

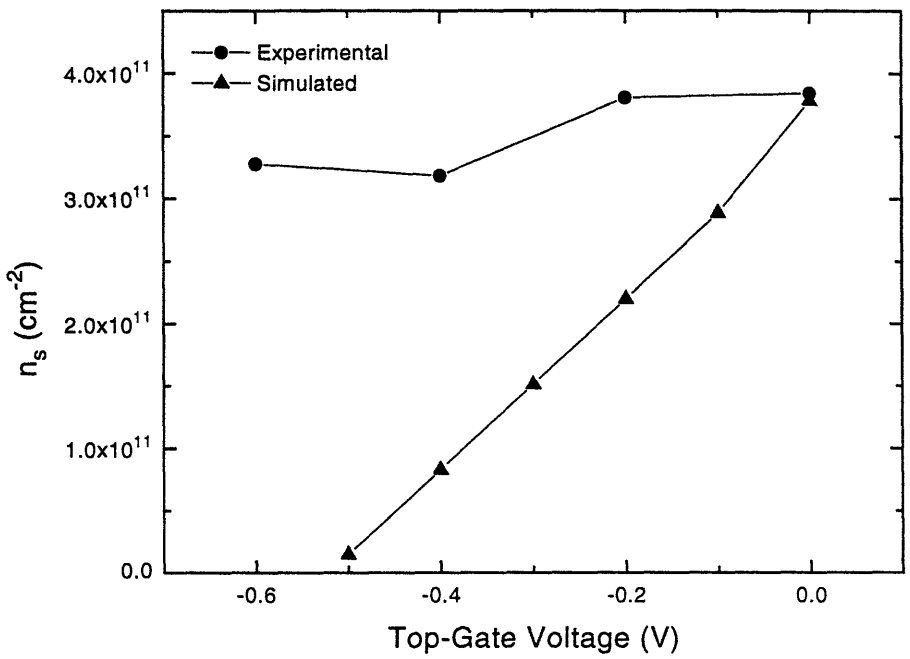

Figure 4-7: n_s for various top-gate voltages in the 2D regime as computed from experimental data and by simulation.

under the gate. However, this edge channel can still conduct through the split-gate gap, where the electron concentration has been only slightly depleted sideways by fringing fields. This agrees with studies that show that the source-drain conductance of two quantized regions in parallel is equal to the conductance of the region with the higher Landau level index.[16]

4.3.2 1D Regime

The magnetoconductance characteristics of the 1D regime were discussed in Section 2.3. Three magnetic field regimes, the boundaries of which depend on gate voltage, are predicted. For gate voltages in the 1D regime, three regimes are evident in Fig. 3-8 as a function of magnetic field. The conductance is nearly constant at low fields, falls off, then displays plateaus at high fields.

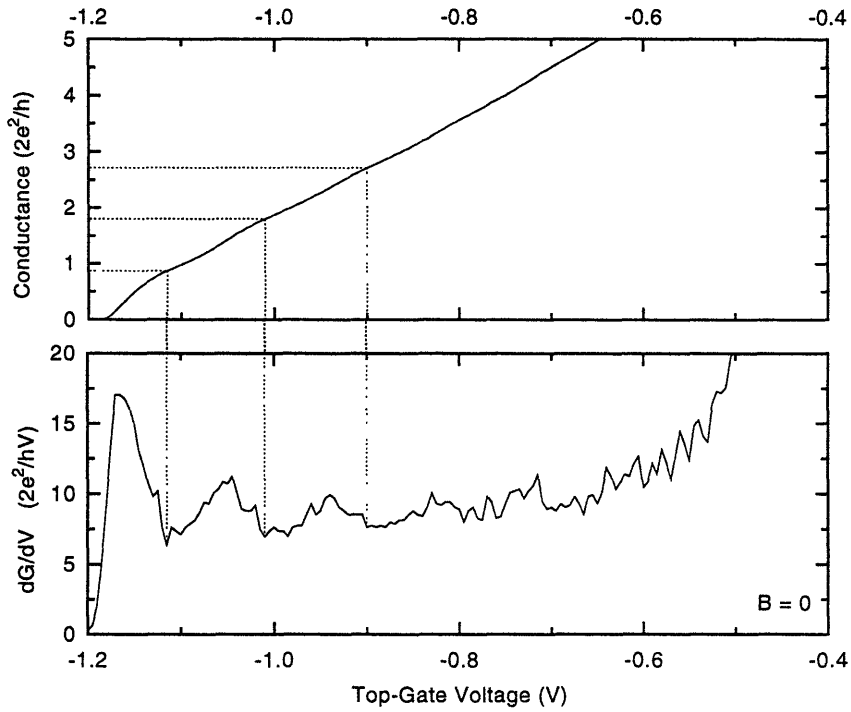

Figure 4-8: Derivative of conductance with respect to top-gate voltage for the second experimental run.

Low-field Regime

For low-fields, conductance is not affected, except for the quantized steps, which become more accurately quantized as discussed in Section 2.3.2. Figs. 3-5 and 3-6 show that low magnetic fields do not affect the structure of the conductance steps and Fig. 3-8 shows that the conductance at a given gate voltage is constant for low fields.

As mentioned above, the quantization of the steps should become more accurate as backscattering is suppressed with increasing field. This can be seen from a plot of step height versus magnetic field. To minimize ambiguity, the step height has been defined as the value of the conductance at the gate voltages at which the derivative of the conductance with respect to gate voltage is minimum (where the conductance curve is flattest). For illustration, Fig 4-8 shows conductance and the derivative of conductance versus gate voltage at zero magnetic field for the second experimental run. The three conductance plateaus occur at $V_{tg} \approx$ -1.1 V, -1.0 V, and -0.9 V. and the corresponding conductances at these gate voltages are the plateau heights.

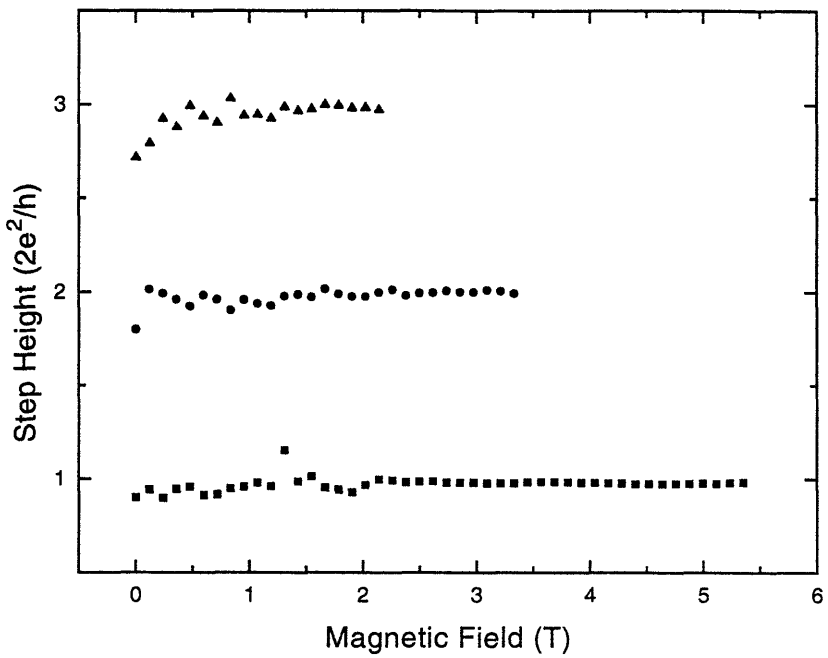

Figure 4-9: Step height versus magnetic field for the second experimental run.

Fig. 4-9 is a plot of step height versus magnetic field for the second experimental run. As shown in this figure, the step height is inaccurate at low magnetic fields and becomes more accurate as the field is increased. In the highest fields, the steps are within an average of 0.9 percent of their ideal values. The step heights are still not expected to be exactly equal to integral multiples of $\frac{2e^2}{h}$ due to series resistance.[4,10]

Magnetic Depopulation Regime

In the magnetic depopulation regime, the cyclotron orbit is on the order of the waveguide width and the magnetic field starts affecting the conductance in a significant way. The conductance steps widen and the number of steps at a given gate voltage drops as the field is increased. This is evident in our experiments in Figs. 3-5, 3-6, and 3-7. The conductance at a given gate voltage begins to decrease with increasing field (decreasing $1/B$) as shown in Fig. 3-9. This figure also shows that the magnetic field at which the conductance begins to decrease is dependent upon gate voltage.

As the magnetic field is increased, the gate voltage needed to depopulate a subband increases as discussed in Section 2.3.3. This can be seen in a plot of the top-gate

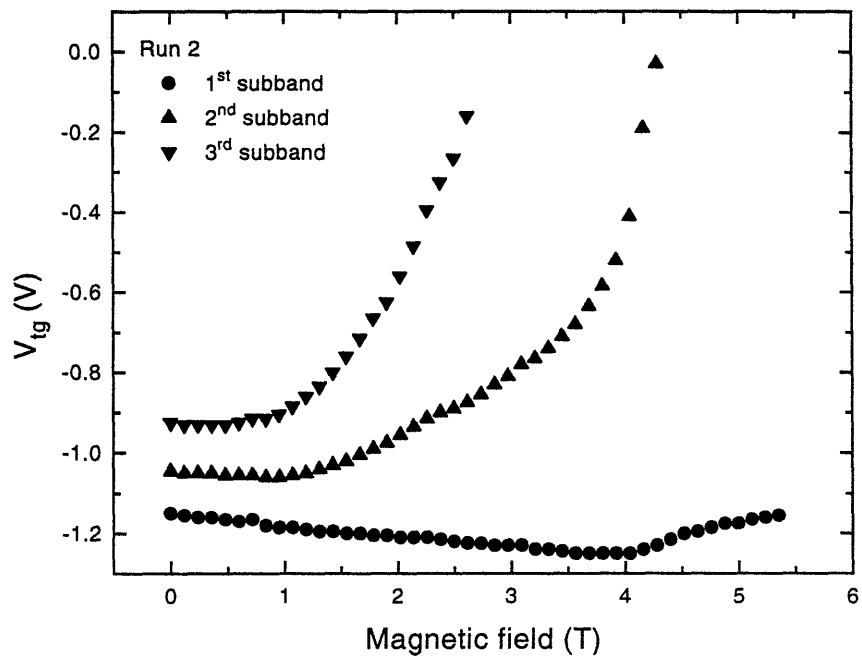

Figure 4-10: Top-gate voltage versus magnetic field for the onset of subbands for the second experimental run.

voltage for the onset of a subband versus magnetic field. The onset of the nth subband is defined as the point where the conductance is equal to $(n - \frac{1}{2})\frac{2e^2}{h}$, halfway between the $(n-1)^{th}$ and the nth plateau. Figs. 4-10 and 4-11 plot the gate voltage versus magnetic field for the onset of subbands for the second and third experimental runs. As mentioned in Chapter 3, a shift in threshold voltage occurs in both experiments. In the second experimental run, the prominent negative threshold shift also shifts the onset of the first subband.

Neglecting the threshold shifts, both plots show that the subband onset voltages are constant at low fields, but begin to rise beyond a certain field that depends on each subband. These plots also show that the boundaries of the magnetic depopulation regime depend upon gate voltage. For more negative gate voltages, the electrostatic confinement is stronger, the waveguide is narrower, and larger fields are needed to begin depopulation.

Using a parabolic approximation for the electrostatic potential, we have analyzed the experimental data in Figs. 4-10 and 4-11, and calculated both the 1D electron

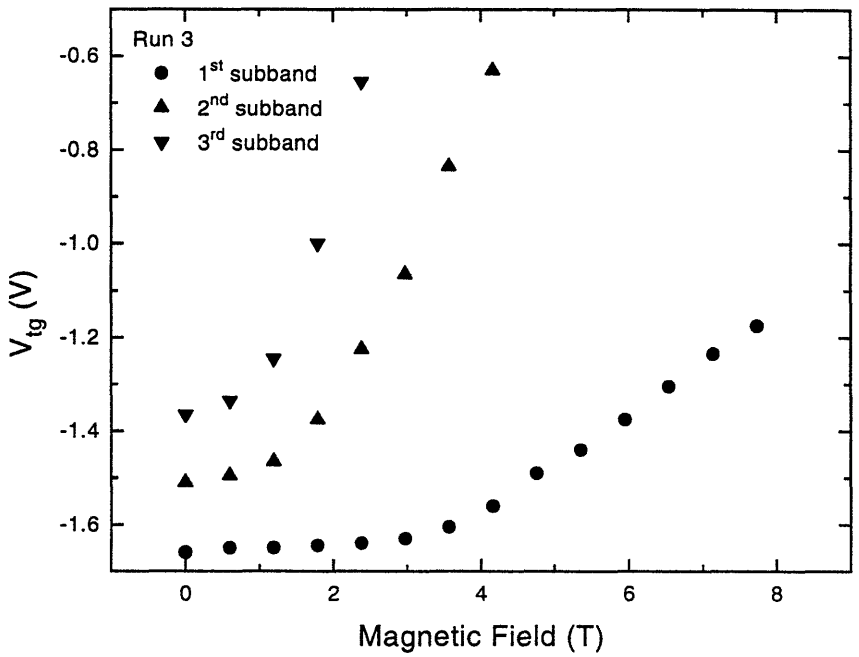

Figure 4-11: Top-gate voltage versus magnetic field for the onset of subbands for the third experimental run.

concentration in the waveguide and the position of the Fermi level. This analysis proved inconclusive and shows that a more complicated potential such as the flat-bottomed well with parabolic sides[11,10] is required to match the experiments.

Quantum Hall Regime

In the quantum Hall regime, the cyclotron orbit is much smaller than the width of the waveguide and the conductance behavior is the same as the 2D behavior. Therefore, conductance is quantized with magnetic field at integral values of $\frac{2e^2}{h}$ as shown in Fig. 3-9 and the plateau index should be linearly dependent upon inverse magnetic field. Fig. 4-12 plots plateau index versus inverse magnetic field for top-gate voltages in the 1D regime. Above a certain field that depends upon the gate voltage, the data points lie on a straight line that crosses the origin, just as in the 2D case (Fig. 4-6). This linear relationship between plateau index and inverse magnetic field is the key signature of the quantum Hall regime and shows that the waveguide indeed enters the quantum Hall regime at high fields.

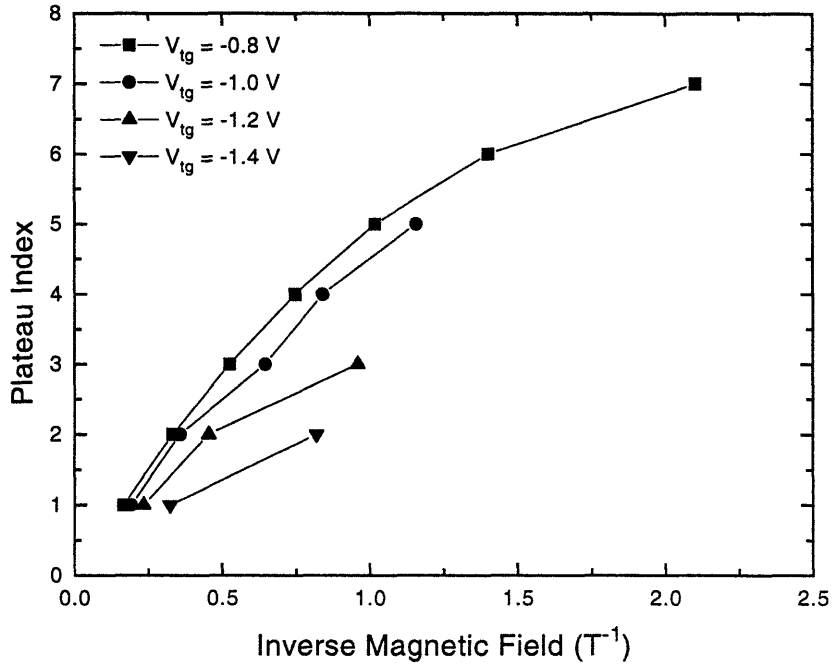

Figure 4-12: Plateau index versus inverse magnetic field for top-gate voltages in the 1D regime.

4.4 Summary

In this chapter, we have simulated a typical electron waveguide, calculated the conductance predicted by the simulation as a function of gate voltage, and examined the simulated potential shape. We found that the simulated potential is more like a parabolic well than a square well. Finally we compared the theoretical, experimental, and simulated predictions in the various gate voltage and magnetic field regimes. In the 2D classical Hall regimes, we explored geometric issues and found that theoretical and experimental conductance behavior are in reasonable agreement. For non-zero gate voltages in the 2D quantum Hall regime, theoretical and experimental predictions of n_s differ from simulated results, but this is explained using the edge state model. In the 1D regime, although no conclusive quantitative analysis is performed, experimental results agree qualitatively with theoretical predictions. Experiments clearly show increased quantization at low-fields, magnetic-field-induced depopulation in medium fields, and quantum Hall behavior in high fields, thus confirming the three theoretically predicted magnetic field regimes.

Chapter 5

Conclusion

As device dimensions are scaled down to the order of the electron mean free path, the wave nature of electrons becomes prominent and a ballistic quantum-mechanical transport model must be used to describe devices. When a magnetic field is applied to such a reduced-dimensionality system, the electrons become magnetically confined and many interesting physical phenomena occur. Thus, magnetic field measurements provide an additional way to study electron physics. Electron waveguides, which have 2D and 1D regimes of operation have been used to study the physics of reduced-dimensional systems. This thesis has presented a study of the magnetotransport in electron waveguides.

Theoretical analysis predicts three magnetic field regimes in the 2D regime and three magnetic field regimes in the 1D regime. In the 2D regime, the three magnetic field regimes are the low-field classical Hall regime, the high-field classical Hall regime, and the quantum Hall regime. In the low-field classical Hall regime, the cyclotron radius is much larger than the mean free path of electrons and the energy spacing of the Landau levels is much smaller than the thermal smearing of the Fermi function. In this regime, the two-terminal conductance is not affected by the magnetic field and is given by the zero-field two-terminal conductance. In the high-field classical Hall regime, the cyclotron radius is much smaller than the mean free path but the Landau level spacing is still smaller than Landau level broadening and smearing. The conductance in this regime is a geometric mix of the longitudinal and transverse

conductances that depend upon the magnetic field. In the quantum Hall regime, the Landau level spacing is much greater than the Landau level broadening. The conductance in the quantum Hall regime is quantized at integral multiples of $\frac{2e^2}{h}$ and is periodic in $1/B$.

In the 1D regime, there are also three magnetic field regimes: the low-field regime, the magnetic depopulation regime, and the quantum Hall regime. The cyclotron radius is much larger than the width of the waveguide in the low-field regime and the conductance is again given by the zero-field conductance. Reduction of backscattering by the magnetic field should reduce series resistance and increase the accuracy of quantization as the field is increased. In the magnetic depopulation regime the cyclotron radius is comparable to the width of the waveguide and the magnetic field affects conductance by providing additional confinement for electrons in the waveguide and depopulating the subbands. In the quantum Hall regime, the cyclotron radius is much smaller than the width of the waveguide and magnetic confinement dominates so the device exhibits the same conductance behavior as in the 2D regime.

We performed measurements of conductance versus gate voltage for various magnetic fields and versus magnetic field for various gate voltages on an electron waveguide fabricated[3] on an AlGaAs/GaAs modulation-doped heterostructure.[2] We also simulated a typical electron waveguide using a self-consistent Poisson/Schrodinger solver,[14] calculated the conductance predicted by the simulation as a function of gate voltage, and examined the simulated potential shape. Finally, we compared theoretical, experimental and simulated results in the various gate voltage and magnetic field regimes.

In the 2D regime, we found qualitative experimental evidence of three magnetic field regimes. In fairly good agreement with theoretical expectations, the 2D conductance is constant for low fields, then begins to fall off as the magnetic field is increased. At higher fields, the conductance shows periodic behavior in inverse magnetic field and becomes quantized at integer values of $\frac{2e^2}{h}$. In the classical Hall regimes, we explored geometric issues and found that the theoretical and experimental conductance are in reasonable agreement. For non-zero gate voltages in the quantum Hall regime,

theoretical and experimental predictions of n_s differ from simulated results, but this is easily explained using the edge state model of the quantum Hall effect.

In the 1D regime, we also see qualitative evidence of three magnetic field regimes in our experimental data. Conductance is quantized in gate voltage and its structure is unaffected by small magnetic fields. We have observed a theoretically predicted increase in the quality of quantization of conductance plateaus as the field is increased. Eventually, the conductance plateaus begin to widen and flatten at high fields. A plot of conductance versus magnetic field is constant for low fields and eventually begins to decrease as the field is increased. At high fields, as in the 2D regime, the conductance becomes periodically quantized at integer values of $\frac{2e^2}{h}$ with magnetic field, which is the key signature of the quantum Hall regime. Quantitative modeling of magnetoconductance in the the 1D regime is difficult because it demands a detailed understanding of the shape of the electrostatic potential and its evolution with gate voltage, which is difficult to determine. Although we have not performed such a quantitative analysis, we have presented clear experimental evidence of the three magnetic field regimes.

Bibliography

[1] G. Timp, in "Semiconductors and Semimetals, Volume 35: Nanostructured Systems (M.Reed, ed.)," Academic Press, San Diego (1992.)

[2] M.R. Melloch, D.C. Miller, and B. Das, "Effect of a GaAs buffer layer grown at low substrate temperatures on a high-electron-mobility modulation-doped two-dimensional electron gas," *Appl. Phys. Lett.* **54**(10), 943 (1989).

[3] C.C. Eugster, "Electron waveguide devices," Ph.D. Thesis, 1993.

[4] B.J. van Wees, H. van Houten, C.W.J. Beenakker, J.G. Williamson, L.P. Kouwenhoven, D. van der Marel, and C.T. Foxon, "Quantized conductance of point contacts in a two-dimensional electron gas," *Phys. Rev. B* **60**(9), 848 (1988).

[5] D.A. Wharham, T.J. Thornton, R. Newberry, M. Pepper, H. Ahmed, J.E.F. Frost, D.G. Hasko, D.C. Peacock, D.A. Ritchie, and G.A.C. Jones, "One-dimensional transport and the quantisation of the ballistic resistance," *J. Phys. C* **21**, L209 (1988).

[6] T. Ando, A.B.Fowler, and F.Stern, "Electronic properties of two-dimensional systems," *Rev. Mod. Phys.* **54** (2), 437 (1982).

[7] K. von Klitzing, "The quantized Hall effect," *Rev. Mod. Phys.* **58** (3), 519 (1986).

[8] R.B. Laughlin, "Quantized Hall conductivity in two dimensions," *Phys. Rev. B* **23**(10), 5632 (1981).

[9] B.J. van Wees, L.P. Kouwenhoven, H. van Houten, C.W.J. Beenakker, J.E. Mooij, C.T. Foxon, and J.J. Harris, "Quantized conductance of magnetoelectric subbands in ballistic point contacts," *Phys. Rev. B* **38**(5) 3625 (1988).

[10] D.A. Wharham, U. Ekenberg, M. Pepper, D.G. Hasko, H. Ahmed, J.E.F. Frost, D.A. Ritchie, D.C. Peacock, and G.A.C. Jones, "Empirical relation between gate voltage and electrostatic potential in the one-dimensional electron gas of a split-gate device," *Phys. Rev. B* **39**(9), 6283 (1989).

[11] K.F. Berggren and D.J. Newson, "Magnetic depopulation of electronic subbands in low-dimensional semiconductor systems and their influence on the electrical resistivity and Hall effect," *Semicond. Sci. Technol.* **1**, 327 (1986).

[12] B.J. van Wees, L.P. Kouwenhoven, E.M.M. Willems, C.J.P.M. Harmans, J.E. Mooij, H. van Houten, C.W.J. Beenakker, J.G. Williamson, and C.T. Foxon, "Quantum ballistic and adiabatic electron transport studied with quantum point contacts," *Phys. Rev. B* **43**(15), 12451 (1991).

[13] C.W.J. Beenakker and H. van Houten, "Skipping orbits, traversing trajectories, and quantum ballistic transport in microstructures," *Superlattices and Microstructures* **5**(1), 127 (1989).

[14] G.L. Snider, I.-H. Tan, and E.L. Hu, "Electron states in mesa-etched one-dimensional quantum well wires," *J. Appl. Phys.* **68**(6), 2849(1990).

[15] N.W. Ashcroft and N.D. Mermin, "Solid State Physics," W.B. Saunders Company, Philadelphia, 1976.

[16] D.A. Syphers and P.J. Stiles, "Contiguous two-dimensional regions in the quantized Hall regime," *Phys. Rev. B* **32**(10), 6620 (1985).

[17] S.L. Park, "The anomalous magnetoresistance of the electron gas in a restricted geometry," Ph.D. Thesis, 1978.

[18] P.F. Bagwell and T.P. Orlando, "Landauer's conductance formula and its generalization to finite voltages," *Phys. Rev. B* **40**(3), 1456 (1989).

[19] F.F. Fang and P.J. Stiles, "Quantized magnetoresistance in two-dimensional electron systems," *Phys. Rev. B* **27**(10), 6487 (1983).

[20] T.G. Powell, C.C. Dean, and M. Pepper, "Two-terminal conductance of the quantised Hall resistor," *J. Phys. C* **17**, L359 (1984).

[21] B.I. Halperin, "Quantized Hall conductance, current-carrying edge states, and the existence of extended states in a two-dimensional disordered potential," *Phys. Rev. B* **25**(4), 2185 (1982).

[22] H. van Houten, C.W.J. Beenakker, P.H.M. van Loosdrecht, T.J. Thornton, H. Ahmed, M. Pepper, C.T. Foxon, and J.J. Harris, "Four-terminal magnetoresistance of a two-dimensional electron-gas constriction in the ballistic regime," *Phys. Rev. B* **37**(14), 8534 (1988).

[23] M.R. Melloch, private communication.

[24] M.J. Rooks, C.C. Eugster, J.A. del Alamo, G.L. Snider, and E.L. Hu, "Split-gate electron waveguide fabrication using multilayer poly(methylmethacrylate)," *J. Vac. Sci. Technol. B* **9**(6), 2856 (1991).

[25] C.C. Eugster, J.A. del Alamo, P.A. Belk, and M.J. Rooks, "Criteria for the observation of one-dimensional transport in split-gate field-effect quantum wires," *Appl. Phys. Lett.* **58**(25), 2966 (1991).

[26] T. Usuki, M. Takatsu, M. Saito, M. Okada, and N. Yokoyama, "Numerical analysis for mesoscopic electron wave devices emplying high-mobility 2D electron gas," *paper presented at Second International Symposium on New Phenomena in Mesoscopic Physics, Hawaii, Dec. 7-11, (1992).*

[27] C.W.J. Beenakker and H. van Houten, in "Solid State Physics, Volume 44: Semiconductor Heterostructures and Nanostructures (H. Ehrenreich and D. Turnbull, eds.)," Academic Press, San Diego (1991).